Title

Encoding Growth Factor Identity in the Temporal Dynamics of FOXO3 under the Combinatorial Control of ERK and AKT Kinases

Journal

Cell Systems, 6(6)

ISSN

2405-4712

Authors

Sampattavanich, Somponnat
Steiert, Bernhard
Kramer, Bernhard A
et al.

Publication Date

2018-06-01

DOI

10.1016/j.cels.2018.05.004

Peer reviewed

HHS Public Access

Author manuscript

Cell Syst. Author manuscript; available in PMC 2019 June 27.

Published in final edited form as:

Cell Syst. 2018 June 27; 6(6): 664–678.e9. doi:10.1016/j.cels.2018.05.004.

Encoding growth factor identity in the temporal dynamics of FoxO3 under the combinatorial control of ERK and AKT Kinases

Somponnat Sampattavanich[1,2], **Bernhard Steiert**[1,3,4], **Bernhard A. Kramer**[1,5], **Benjamin M. Gyori**[1], **John G. Albeck**[6], and **Peter K. Sorger**[1,7]

[1] HMS LINCS Center and Laboratory of Systems Pharmacology, Department of Systems Biology, Harvard Medical School, 200 Longwood Ave, Boston, USA [2] Siriraj Laboratory for Systems Pharmacology, Department of Pharmacology, Faculty of Medicine Siriraj Hospital, Mahidol University, Bangkok, Thailand [3] Institute of Physics, University of Freiburg, Freiburg, Germany [4] Freiburg Center for Systems Biology, University of Freiburg, Freiburg, Germany [5] Division of Systems Biology of Signal Transduction, German Cancer Research Center, Heidelberg, Germany [6] Department of Molecular and Cellular Biology, University of California, Davis, USA [7] Lead Contact

SUMMARY

Extracellular growth factors signal to transcription factors via a limited number of cytoplasmic kinase cascades. It remains unclear how such cascades encode ligand identities and concentrations. In this paper we use live-cell imaging and statistical modeling to study FoxO3, a transcription factor regulating diverse aspects of cellular physiology that is under combinatorial control. We show that FoxO3 nuclear-to-cytosolic translocation has two temporally distinct phases varying in magnitude with growth factor identity and cell type. These phases comprise synchronous translocation soon after ligand addition followed by an extended back and forth shuttling; this shuttling is pulsatile and does not have a characteristic frequency, unlike a simple oscillator. Early and late dynamics are differentially regulated by Akt and ERK and have low mutual information, potentially allowing the two phases to encode different information. In cancer cells in which ERK and Akt are dysregulated by oncogenic mutation, the diversity of states is lower.

eTOC Blurb:

Please address correspondence to: • Peter Sorger, WAB Room 438 Harvard Medical School, 200 Longwood Avenue, Boston MA 02115 Tel: 617-432-6901/6902 peter_sorger@hms.harvard.edu, • Somponnat Sampattavanich, 12th Floor Srisavarindhira Building, Siriraj Hospital, 2 Wanglang Road, Bangkoknoi, Bangkok, Thailand 10700 Tel: +6624195248 somponnat.sam@mahidol.edu.

AUTHOR CONTRIBUTIONS

Conceptualization, S.S., P.K.S.; Methodology, S.S., P.K.S., J.A; Investigation, S.S., B.K., Formal Analysis, S.S., B.S., B.G.; Writing P.K.S., S.S, B.S., B.G., J.A.; Funding Acquisition, P.K.S.

DECLARATION OF INTERESTS

None.

Eukaryotic transcription factors frequently oscillate between the nucleus and cytosol. We show that translocation by human FoxO3 is pulsatile rather than oscillatory and subject to combinatorial control by the ERK and Akt pathways. As a result, FoxO3 dynamics can encode the identities and concentrations of diverse extracellular growth factors.

Graphical Abstract

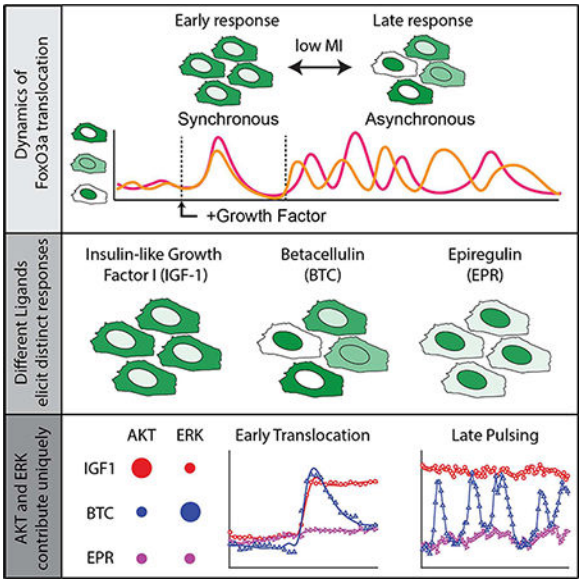

Keywords

Signal transduction; transcription; combinatorial control; FOXO proteins; oncogenes; ERK; AKT

INTRODUCTION

Activation of different growth factor receptors induces distinct phenotypes and cellular responses while engaging a common set of kinase cascades. The Ras/ERK and PI3K/Akt kinase cascades are particularly important in linking transmembrane receptor activity to mitogenic transcription and cell cycle progression. It remains unclear how cells transduce information about receptor occupancy to transcription factors using a limited number of overlapping signal transduction molecules. Some studies suggest that the identity of growth factors is encoded in the dynamics of effector activation (Traverse et al., 1994) or differential activation of ERK and Akt pathways (Chen et al., 2012). Theoretical studies predict that activation of parallel signaling pathways might serve to increase the accuracy of signaling downstream of a receptor input (Cheong et al., 2011).

Signaling kinases and the transcription factors they control often switch between on and off states repeatedly over the course of a 12–24 hour response (Levine et al., 2013; Purvis and Lahav, 2013). Such switching is frequently asynchronous from one cell to the next and best monitored using time-lapse microscopy of fluorescent reporter proteins. Both p53 and NF-κB undergo nuclear/cytosolic translocation in which the duration of the active (nuclear) state

determines promoter selectivity and level of transcription. p53 activation by DNA damage was initially thought to involve a few strongly damped oscillations (Lev Bar-Or et al., 2000) but live-cell imaging reveals extended asynchronous oscillation at a single-cell level (Batchelor et al., 2011; Lahav et al., 2004). Similar long-duration pulsing has been observed for NF-κB following exposure of cells to inflammatory cytokines such as TNF-α (Nelson et al., 2004; Tay et al., 2010).

Pulsing genetic circuits have the potential to encode information in pulse amplitudes, frequencies and duration (Levine 2013). For example, the activity of the extracellular signal regulated kinase ERK, the downstream effector of the mitogen-activated protein kinase (MAPK or MEK/ERK) cascade, is pulsatile when cells are exposed to low concentrations of growth factor. The likelihood that a cell will enter S phase correlates with the duration of the ERK_{ON} state (Albeck et al., 2013). The regulation and coding potential of pulsatile circuits is best understood in single-cell organisms. In yeast, both frequency-modulated (FM) and amplitude- modulated (AM) encoding has been observed for Msn2, a transcription factor involved in general stress response, and the identity and intensity of upstream activators appears to be encoded by FM and AM processes working in tandem (Hansen and O'Shea, 2015). Combinatorial gene regulation is achieved by modulating the relative timing of Msn2 and Mig1 pulses (Mig1 is a transcriptional repressor that controls metabolic genes) (Lin et al., 2015). Eukaryotic cells have long been known to exploit combinatorial transcriptional control but the role of pulsing circuits in such control has only recently become a topic of interest.

The Forkhead box O3 transcription factor (FoxO3) functions as an integrative node for several upstream signaling networks. In mammalian cells, FoxO3 is one of four FoxO family-member proteins implicated in biological processes that include cycle arrest, apoptosis, oxidative stress, cell migration and cell metabolism. Combinations of upstream inputs alter the post-translational modification state of FoxO3 and these changes control abundance, subcellular localization and DNA-binding capacity (Calnan and Brunet, 2008; Eijkelenboom and Burgering, 2013). Mitogenic growth factors negatively regulate FoxO3 activity via the MEK/ERK and the PI3K/Akt kinase cascades (Biggs et al., 1999; Brunet et al., 1999; Yang et al., 2008) whereas oxidative stress exerts positive regulation via the JNK and MST1 kinases (Essers et al., 2004; Lehtinen et al., 2006).

Phosphorylation of FoxO3 by Akt at T32, S253 and S315 promotes interaction with 14–3-3 proteins, causing nuclear to cytosolic translocation and relieving repression of mitogenic genes (Brunet et al., 2002). ERK phosphorylation on S294, S344 and S425 also promotes FoxO3 nuclear-to-cytosolic translocation and degradation via MDM2-dependent ubiquitin-mediated proteolysis (Yang et al., 2008). Other regulators of FoxO3 activity include energy stress via the AMPK pathway (Greer et al., 2007), genotoxic stress via CDK proteins (Huang et al., 2006) and cytokines via the IκB kinase (Hu et al., 2004). Measuring and analyzing such complex signal encoding is fundamental to understanding combinatorial control by FoxO-family transcription factors and may be of diagnostic value in cell types with misregulated FoxO proteins (van der Horst and Burgering, 2007).

In this paper we study how the identities and concentrations of growth factors are encoded in the dynamics of FoxO3 activity. We find that FoxO3 exhibits complex patterns of nuclear-to-cytosolic translocation in ligand-activated cells on multiple time scales. Across all cells in a population, synchronous cytosolic translocation is observed within 20 min of ligand addition, followed by a return to the nucleus and then an extended period of asynchronous (and non-oscillatory) shuffling between cytosolic and nuclear compartments. The relative magnitude of synchronous translocation and pulsing varies with the identity of the activating growth factor and the properties of the cell line with synchronous translocation regulated primarily by Akt and pulsing by Akt plus ERK. Our data provide insight into combinatorial control of FoxO3 by immediate-early signal transduction cascades pathways and demonstrate how a single transcription factor can assume a wide range of possible states in response to different upstream inputs.

RESULTS

Design and characterization of the F3aN400-Venus reporter

FoxO localization has been studied in live mammalian cells using fluorescent protein fusions (Gross and Rotwein, 2015; Senapedis et al., 2011), but the impact of differences in ligand identity and concentration has not been investigated in depth. We therefore constructed a FoxO3 translocation reporter responsive to both ERK and Akt that is not expected to perturb normal transcription (Figure 1A). A Venus fluorescent protein was fused to a 400-residue domain of human FoxO3 containing all three known sites of Akt phosphorylation (T32, S253 and S315; Figure 1A, green text) and two of three known ERK phosphorylation sites (S294 and S344; blue text) but lacking a transactivation domain. The F3aN400-Venus reporter also carried an H212R loss-of-function mutation in the DNA binding domain to prevent dominant negative effects on endogenous FoxO3 (Tran et al., 2002); such effects were observed with a full-length FoxO3 construct. To determine if F3aN400-Venus faithfully captures FoxO3 dynamics, parallel cultures of parental and F3aN400-Venus expressing 184A1 cells were treated with EGF at concentrations from near physiological to saturating (0.4–100 ng/mL) in combination with the allosteric Akt1/2/3 inhibitor MK-2206 at varying doses; this protocol was observed to elicit a wide range of FoxO3 states from fully nuclear localized to fully cytosolic (Figure 1B). F3aN400-Venus was imaged directly and parental cells stained with anti-FoxO3 antibody. When cells were segmented and the median nuclear-cytoplasmic translocation value (median of $\log_{10}(C_{norm}/N_{norm})$) compared for the reporter and endogenous protein, a Pearson's correlation coefficient of 0.91 was obtained, representing a high degree of concordance. The dynamic range estimated for the nuclear-cytoplasmic ratio was similar for endogenous FoxO3 (−0.8 to 0; Figure 1B), and F3aN400-venus (−0.6 to 0.2); as expected, dynamic range varied depending on how background intensity was computed but values were insensitive to the image segmentation algorithm used (see STAR Methods for complete definitions; Figure S1A-D). We conclude that the localization of the F3aN400-venus report and endogenous FoxO3 are similar across a wide range of conditions.

Variability in nuclear-to-cytoplasmic ratio across cells in a culture (as quantified by interquartile range; IQR), serves as a surrogate measurement for shuttling between the

nucleus and cytoplasm in the absence of a reporter (this makes the ergodic assumption that difference across many cells at a single point in time are reflective of differences over time in a single cell; Figure S1E). Across a range of conditions, the median and IQR of the nuclear/cytoplasmic ratio for endogenous FoxO3 and the F3aN400-Venus reporter were similar suggesting that the fluorescent sensor recapitulates most but not all of the dynamics of endogenous FoxO3 (Figure S1F). The largest discrepancy was observed at low levels of cytoplasmic translocation when the endogenous protein is expected to be more completely retained in the nucleus than the reporter because only the former is active in DNA binding. In common with many live-cell studies of transcription factor shuttling, we were unable to distinguish the behavior of FoxO3 that is chromatin bound and FoxO3 that is free in the nucleus. Nonetheless, F3aN400-Venus appears to be a faithful reporter of overall FoxO3 state.

To investigate regulation of F3aN400-Venus by Akt and ERK, serum-starved 184A1 cells were treated with one of six growth factors at 100 ng/mL and the levels of phosphorylated $pAkt^{S473}$ and $pERK^{T202/Y204}$ measured by immunoblotting (phosphorylation at these sites, henceforth pERK and pAkt, is a surrogate for Akt and ERK kinase activity; Figure S1G). IGF1 caused strong and persistent Akt activation whereas EGF, BTC, EPR, HGF and HRG caused transient activation. The opposite pattern was observed for ERK, with EGF eliciting the strongest ERK activity and IGF1 the least. These differences corresponded well to phosphorylation of F3aN400-Venus, as measured by pS294 and pS253 ratios 15–480 minutes after growth factor addition (Figure 1C & Figure S1G). Use of selective kinase inhibitors (MK-2206 for Akt1/2/3 and CI-1040 for MEK1/2) confirmed that F3aN400-Venus phosphorylation was ERK-dependent on S294 and Akt-dependent on S253 (Figure S1G; right-most immunoblot panel), consistent with the well-established biology of FoxO3 (Brunet et al., 2001; Yang et al., 2008). We conclude that the F3aN400-Venus reporter recapitulates previously described patterns of FoxO3 nuclear translocation and phosphorylation.

To study F3aN400-Venus translocation dynamics in response to growth factors, F3aN400-Venus localization was monitored by live-cell microscopy over a 24-hr period. Following exposure to EGF (Figure 1D, red arrowhead), synchronous cytosolic translocation of the reporter was observed in all cells, peaking at t=15–20 minutes, followed by a return to the nucleus by t= 60–100 minutes. Starting at ~80 minutes after EGF addition (Figure 1D, blue arrowhead), shuttling between the cytosol and nucleus was observed every 50–100 minutes. Shuttling was not observed in all cells but, when it did occur, continued for up to 24 hours and was asynchronous from one cell to the next. Immunofluorescence imaging of endogenous FoxO3 in >1000 fixed cells at each time point confirmed translocation from the nucleus to the cytosol in >90% of cells at 10–30 minutes after EGF addition (Figure 1E), followed by a progressive increase in the IQR of $\log_{10}$(C/N) after 30 minutes, consistent with live-cell studies. When 184A1 cells were exposed to one of six growth factors at concentrations ranging from roughly physiological to saturating we found that IGF 1 elicited sustained nuclear-to-cytosolic translocation while the EGF-like growth factors betacellulin (BTC) and epiregulin (EPR) elicited transient translocation followed by varying degrees of pulsing (Figure 2; see also Video S1). Thus, FoxO3 translocation exhibits qualitatively distinct translocation dynamics depending on growth factor.

Synchronous FoxO3 translocation dynamics vary with growth factor dose and identity

To quantify differences in F3aN400 trajectories following growth-factor stimulation of 184A1 cells, >100 trajectories were collected per condition and then separated into early synchronous and a later pulsing phases. For the early synchronous phase, functional principal component analysis (fPCA) was used to decompose the signal prior to and immediately after ligand addition (t = −70 to +80 min) into a weighted set of orthogonal harmonic functions. Three harmonic functions explained >95% of variance across growth factors and doses, representing excellent performance for a PCA model (Figure 3A & Figure S2A). The harmonic corresponding to the first principal component (fPC1) comprised the pre-treatment baseline signal, while fPC2 corresponded to a rapid increase in cytoplasmic-nuclear ratio to a high and constant value by t= 20 minutes; fPC3 was transient, rising rapidly to a maximum at t = 15 minutes and then falling below baseline levels by 75 minutes (Figure 3A). In the landscape of fPC2 vs. fPC3, BTC, IGF1 and EPR represented extrema: BTC scored relatively high in both fPC2 and fPC3, IGF1 scored high in fPC2, and EPR scored low in both fPC2 and fPC3 (Figure 3B). These differences were statistically significant, but other ligands exhibited intermediate behavior and could not be as cleanly distinguished from each other (Figure 3C). For all but IGF1, fPC2 and fPC3 scores varied smoothly with dose (Figure 3D) suggesting that differences in loadings reflect qualitative differences among ligands and not simply varying degrees of receptor activation. Scores for fPC 1 were variable and not significantly different among growth factors whereas fPC2 and fPC3 scores discriminated among ligands with high confidence (Figure S2B; $p<10^{-10}$ based on Wilcoxon rank sum test as compared to unstimulated cells). We conclude that different growth factors induce significantly different FoxO3 translocation dynamics in the initial synchronous phase of response to growth factor.

FoxO3 translocation is pulsatile but not oscillatory

When harmonics comprising fPC1-fPC5 were added together in proportion to their scores, the contribution of long-wavelength changes to F3aN400-Venus dynamics could be visualized (Figure 3E). In the case of EGF we found that this “trend” response comprised both synchronous translocation into the cytoplasm and quick return to the nucleus by t=80 minutes (as described above) as well as gradual return to the cytosol between t= 200 and 300 minutes in a majority of cells (Figure 3E, left panel). Subtracting this trend response from the original trajectories revealed the pulsatile signal (Figure 3E, right panel). When fPCA analysis was performed on trajectories between t= 80 to 1580 minutes the PCA scores were significantly different from those of unstimulated cells only in the case of IGF1. Thus, only IGF1 is associated with a significant “trend” response at later times, consistent with manual inspection showing sustained cytosolic FoxO3 localization. For other ligands, fPCA scores for the late response were insignificantly different from each other and from untreated cells. Reconstructed late-phase trend lines obtained by adding these fPCA harmonics together (Figure S3A) were nonetheless useful in correcting for drift and background fluorescence on a trajectory by trajectory basis.

Oscillation is often observed in dynamical systems having strong feedback regulation (Elowitz and Leibler, 2000; Lahav et al., 2004). A key characteristic of oscillatory systems is stability in the frequency domain (Halford et al., 1973), a property that can be evaluated by

computing spectral density, the distribution of power vs. frequency. A purely sinusoidal oscillator, when sampled in discrete time, gives rise to a narrow spectral density distribution whose width varies with sampling error and signal-to-noise ratio (the blue line in Figure 2B represents an oscillator with a frequency of ~0.2 mHz sampled every 5 min. convolved by measurement noise). However, detrended trajectories for F3aN400-Venus exhibited an inverse relationship between power and frequency in the range of 0.05 to 2 mHz (Figure 2B); this was true when the data was analyzed either in aggregate or ligand-by ligand. Such a relationship is a characteristic of $1/f$ or "pink" noise (where f is frequency), observed in many non-equilibrium physical systems (Hausdorff and Peng, 1996). When the power spectrum was computed for trajectories with the greatest degree of pulsing (see below), we observed a statistically significant deviation from pure $1/f$ behavior at ~0.2 mHz, which corresponds to a wavelength of 80 ± 30 minutes. This accounts for the apparent periodicity of some F3aN400-Venus trajectories. We conclude that the pulsatile component of F3aN400-Venus trajectories is not oscillatory in the conventional sense, although it does have weak periodicity. Irregular pulsing is a feature of both stochastic and chaotic dynamical systems and either or both could be involved in F3aN400-Venus dynamics (Timmer et al., 2000).

FoxO3 pulsing varies with ligand and carries distinct information

Because F3aN400-Venus trajectories were not oscillatory, we quantified shuttling using a "pulse score" schematized in Figure 4A (and described in full in STAR Methods). This score comprised a nonlinear combination of (1) the number of pulses, (2) the average interval between pulses, (3) the signal-to-noise ratio in the images and (4) the pulse amplitude. We quantified the fraction of pulsing cells in different conditions using a threshold of ~0.6 in pulse score, which optimally discriminated trajectories in cells exposed to BTC and IGF1 (the least and the most pulsatile trajectories as judged by the human eye; Figure 4A). We found that the fraction of pulsing cells rather than pulse amplitude or duration varied the most between conditions, justifying our use of discretization (Figure 4B & Figure S3B). Approximately 10% of serum-starved 184A1 cells exhibited pulsing in the absence of growth factor (Figure 4B; "0 ng/mL"); addition of IGF1 suppressed baseline pulsing in a dose- dependent manner by inducing persistent cytosolic translocation. In contrast, the other five growth factors increased the fraction of pulsing cells above the baseline. Exposure of cells to BTC, HGF or HRG resulted in a progressive increase in the fraction of pulsing cells over a ~ 40-fold concentration range (Figure 4B; blue, green and yellow lines), whereas exposure to EGF or EPR resulted in a sudden increase in pulsing over a narrow ~2- fold range in ligand concentration (cyan and pink). Similar data were obtained in F3aN400-Venus expressing MCF10A cells, a second non-transformed mammary epithelial cell line, except that these cells were less sensitive to BTC and more sensitive to EGF than 184A1 cells (Figure S4B). We conclude that differences in identities and concentrations of an extracellular ligand result in consistent differences in FoxO3 translocation dynamics, as expected for dynamical encoding.

To determine whether the trend and pulsatile components of FoxO3 translocation dynamics carry different information (Hansen and O'Shea, 2015), we calculated the mutual information between fPCA scores for the synchronous response between t= −70 to 80

minutes and the discretized pulse scores between 80–1580 minutes. Variation in early fPCA scores typically explained <20% of the variation in the late pulsatile response and was ligand dependent (Figure 4C; Figure S3C). In this context, this represents a low level of mutual information since trajectories from IGF1-treated cells, in which pulsing is low, exhibited over 60% mutual information between early and late phases (Figure S3C). These data suggest that early and late FoxO3 translocation dynamics are largely independent of each and therefore have the potential to encode different information (except in the case of IGF 1 in which little pulsing is observed).

Regulation of FoxO3 dynamics by Akt and ERK

Information is transduced from transmembrane receptors to FoxO3 via cytosolic kinase cascades, among which those involving Akt and ERK are best understood. Previous work from our group has shown that growth factors differentially activate ERK and Akt signaling in mammary cells (Niepel et al., 2014) and blotting for FoxO3 phosphorylation on S253 and S294 confirmed that differences in kinase activity are transmitted to the F3aN400-Venus sensor (Figure 1C). To investigate the functions of posttranslational modification we engineered threonine to alanine mutations into the F3aN400-Venus sensor at known phosphorylation sites (Figure S4A). Translocation dynamics were quantified by fPCA in the early phases (from −70 to 80 min) and pulse score in the late phase (from 80 to 1580 min). In 184A1 cells, a triple point mutation in Akt sites (T32A/S253A/S315A) totally inhibited cytosolic translocation under all conditions, reducing fPC2 and fPC3 scores to near zero and also eliminating pulsing (Figure 5A). In contrast, mutation of ERK-specific sites (S294A/S344A) had a relatively small effect on either fPCA scores or pulsing, and differences among ligands were retained (Figure 5A). Akt inhibition with MK-2206 phenocopied T32A/S253A/S315A mutation by eliminating all cytosolic translocation and pulsing (Figure 5B). Similar data were obtained in F3aN400-Venus expressing MCF10A cells (Figure S4B).

To further investigate the role of MEK/ERK signaling in pulsing, 184A1 and MCF10a cells were exposed to PD0325901 and EGF in combination over a range of concentrations and pulse score was measured (Figure 5C). In both cell types low-dose MEK inhibitor increased pulse scores above the level observed with EGF alone (to a maximum of 0.8) but as drug concentration increased above 2 nM, pulse score then fell monotonically to a minimum of ~0.3. Because CI-1040 and PD0325901 are among the most selective kinase inhibitors known (they are non ATP-competitive) off-target effects are unlikely. We conclude that MEK and ERK are likely to regulate F3aN400-Venus pulsing indirectly or via unmapped modification sites.

To examine the interplay between pulsing and early synchronous translocation, cells were exposed to growth factors in combination with inhibitors of Akt or MEK inhibitors over a range of concentrations. Dynamics were then analyzed on a landscape of early fPC2 score vs pulse score. In 184A1 cells treated with IGF1, fPC2 score varied with ligand dose, pulse score was low, and addition of Akt inhibitor resulted in a dose-dependent shift along the fPC2 axis, showing that IGF1 primarily regulates FoxO3 via Akt (Figure 5D, orange and yellow data points). Exposure of cells to different levels of EGF changed both fPC2 and pulse scores (Figure S5A; this was true of other ligands as well; Figure S5B). Complete

inhibition of the Akt pathway reduced fPC2 and pulse score to zero (Figure S5A; black square dot). The effects of MEK inhibition were more complex: in 184A1 cells exposed to 20 ng/mL EGF, MEK inhibitor increased pulsing two-fold at intermediate drug concentrations and then reduced it at higher concentrations. At lower EGF concentrations, progressively higher doses of MEK inhibitor resulted in a monotonic decrease in pulsing. Taken together, these data suggest that (i) complete inhibition of Akt blocks cytosolic translocation of F3aN400-Venus under all conditions, (ii) partial inhibition of Akt suppresses both the trend and pulsing responses, (iii) pulsing is also regulated by MEK/ERK signaling, although not via known sites of FoxO3 modification, and (iv) at high ligand levels, fractional inhibition of MEK/ERK can increase pulsing implying that signaling is saturated.

FoxO3 integrates ERK and Akt dynamics

To study the relationship between ERK and FoxO3 dynamics in single cells we constructed a dual reporter in which F3aN400-mCherry was linked to EKAREV, a FRET-based reporter of ERK kinase activity (Albeck et al., 2013; Aoki et al., 2013), via a type 2A self-cleaving peptide (Figure 6A). Trajectories were normalized using trend lines derived from fPCA or spline-fitting and scaled individually by the max-min range for that reporter (to correct for differences in reporter-intrinsic intensity and dynamic range). In MCF10A cells we found that ERK activity and nuclear-to-cytosolic translocation of F3aN400-mCherry cells tracked each other before and after stimulation with BTC (typical pairs of F3aN400 and EKAREV activity trajectories are shown in the upper left panel of Figure 6B; more examples are shown in Figure S6). Across a set of ~30 F3aN400 and EKAREV trajectories, a median Pearson's correlation coefficient of R ~0.83 was obtained for the two trajectories using a sliding 90-minute window (Fig 6B, upper right panel). When cells were stimulated with BTC for 4 hr and then treated with the Akt inhibitor (1μM of MK2206), F3aN400-mCherry stopped pulsing, but EKAREV dynamics were not appreciably altered, causing the two trajectories to decorrelate (median R = −0.03; Figure 6B, middle panels). When BTC-stimulated cells were treated with MEK inhibitor (1μM of CI1040) at t=4 hr, pulsing by both EKAREV and F3aN400-mCherry was largely eliminated and trajectories became decorrelated (median R = 0.17; Figure 6B, bottom panels). We conclude that the EKAREV and F3aN400-mCherry undergo synchronous pulsing in a manner that requires both Akt and ERK activity. When growth factors were compared, EKAREV and F3aN400-mCherry were most highly correlated when pulse scores were high (e.g. with BTC, EPR and EGF as ligands; $p < 0.01$ using Wilcoxon rank sum test against unstimulated cells) and least correlated when pulse scores were low (e.g. with IGF1; Figs. 6C and 6D). Thus, FoxO3 pulsing appears to originate from the dynamics of ERK activity while also requiring activation of the Akt pathway.

Exploring the connectivity of ERK, Akt and FoxO3 in breast cancer cell lines

To determine how FoxO3 translocation varies across cell lines, we selected, from a panel of widely studied breast cancer cells, seven lines that include $HER2^{AMP}$, hormone-receptor positive, and triple negative subtypes (the ICBP43 set (Li et al., 2013)); 184A1 and MCF10A cells were included as examples of normal mammary epithelial controls. Mutations in mitogenic signaling networks are common in breast cancer, and multiple cell

lines in our collection carry oncogenic mutations in HRAS, KRAS, BRAF and PIK3CA. To study FoxO3 localization in these cells we used fixed cell immunofluorescence at 7 time points 15 to 240 minutes following exposure of cells to one of seven growth factors at 100 ng/mL. The average level of FoxO3 activation was captured by the median value of the FoxO3 C/N ratio; the median IQR of the C/N ratio served as a proxy for pulsing compatible (as described above; Figure 7A). Across all ligands and time-points, normal mammary 184A1 and MCF10A exhibited the widest range of signaling states whereas breast cancer cells exhibited narrower ranges (Figure 7B). BT20 and T47D cell lines, which carry activating mutations in the catalytic p85 subunit of PI3K *(PIK3CA),* were confined to the fully active state (high C/N ratio) even in the absence of ligand whereas $BRAF^{G464V}$/ $KRAS^{G13D}$ MDA231 cells exhibited intermediate median C/N ratios and low IQR, suggesting reduced pulsing (Figure 7B). We infer that activating mutations in either the Akt or ERK pathways reduce the accessible dynamic range over which FoxO3 can respond to growth factors.

Based on current understanding of immediate-early signaling, ERK could either regulate FoxO3 directly by phosphorylating it on S294, S344 or S425 (Yang et al., 2008) or it could act indirectly via negative cross-talk on Akt (Moelling et al., 2002; Yu et al., 2002). To begin to distinguish between these possibilities we measured cross-regulation between ERK and Akt in different cell lines exposed to one of seven growth factors. The effect of MEK/ERK on AKT was assessed by measuring $pAkt^{S473}$ levels in the presence and absence of MEK inhibition and the effect of AKT on MEK/ERK by $pERK^{T202/pY204}$ levels was measured in the presence and absence of Akt inhibition (Figure 7C-E). This experiment revealed a wide range of possible interactions between Akt and ERK depending on ligand and cell type. For example, inhibition of Akt with MK2206 following IGF1 exposure significantly increased $pERK^{T202/pY204}$ levels in 184A1 cells but had little effect in MCF10A cells (Figure 7D).

We then used dynamic Bayesian network analysis (Friedman et al., 2000; Hill et al., 2012) to infer the connectivity of ERK, Akt and FoxO3 as assessed by either the median or IQR of the C/N ratio under 32 different conditions (4 inhibitor conditions × 8 ligand conditions) for each cell line (Figure S7A). We found that the probability of edges corresponding to Akt→ FoxO3, ERK → FoxO3 and Akt ↔ERK varied to a significant degree with cell line and ligand (Figure 7F). Probability values also varied with the learning method, as expected for probabilistic analysis of noisy data, but overall agreement was quite good: BGe and BDe scoring algorithms exhibited 94% and 81% agreement with DBN results (Figure S7B-D), suggesting that inferred edge probabilities are likely to be reliable in aggregate (Heckerman et al., 1995b). In all cell lines we found strong evidence of an Akt → FoxO3 interaction, and in HCC1806, HS578T, BT20 and T47D the probability of an ERK → FoxO3 interaction was high. Akt ↔ ERK interactions were strongest in MCF7 cells (Figure 7F). Comparison of FoxO3 translocation in MCF10a and HCC1806 cells exemplified this difference. ERK ^ FoxO3 interaction was inferred to be substantially stronger in HCC1806 than MCF10 cells and MEK inhibition had a substantially greater effect on the distribution of FoxO3 C/N values in HCC1806 than MCF10a cells (Figure 7G). We conclude that networks regulating FoxO3 differ in topology from one cell type to the next and that ERK can probably control pulsing via both Akt-dependent and Akt-independent mechanisms.

DISCUSSION

In this paper we analyze the temporal regulation of FoxO3, a mammalian transcription factor controlled in a combinatorial manner by multiple signal transduction pathways. We focused on nuclear-cytosolic translocation induced by growth factors and its regulation by the ERK and Akt kinase cascades. Relocalization plays an important role in the regulation of transcription factors and has recently been shown by live cell imaging to involve pulses of active and inactive states. In the case of mammalian transcription factors such as NF-kB and p53 (Batchelor et al., 2008; Tay et al., 2010) and yeast Msn2 and Crz1 (Cai et al., 2008; Hao and O'Shea, 2011), modulation of the timing and duration of nuclear-cytosolic translocation carries information about the strength and identity of the initiating stimulus (Hansen and O'Shea, 2016; Tay et al., 2010). We build on these concepts by demonstrating that FoxO3 dynamics comprise early and late phases that respond independently to differences in the relative activities of ERK and Akt kinases, which are determined in turn by growth factor identity and concentration (all data are available for reanalysis in an NIH LINCS format at http://lincs.hms.harvard.edu/sampattavanich-cellsyst-2018/). The early FoxO3 response to ligand is synchronous across all cells and relatively short-lived; the late phase is pulsatile and can last for 24 hr or more. The synchronous response is strongest for ligands such as IGF and weakest for EPR and BTC; the opposite is true of the pulsatile response. These features of FoxO3 appear to be reflective of the interplay between ERK and Akt signaling and provide FoxO3 with significant information encoding capacity. Although we have not yet linked differences in FoxO3 dynamics to differential transcriptional activity, we speculate that the diversity of dynamical responses is relevant to the diverse biological activities of FoxO class of transcription factors.

Ligand identity is transmitted by relative Akt and ERK activities and encoded in FoxO3 dynamics

Across a wide range of ligand types and concentrations, FoxO3 translocation dynamics have two distinct temporal phases. Within 15–20 minutes of growth factor addition, FoxO3 moves from the nucleus to the cytoplasm in near-synchrony across all ligand-activated cells in the population. FoxO3 then shuttles back and forth between the two compartments for up to 24 hr. Early synchronous translocation of FoxO3 appears to be regulated primarily by the intensity of Akt activity. Subsequent pulsing is asynchronous and occurs in phase with pulses of ERK activity; when Akt is active, pulses of ERK activity correspond to periods of FoxO3 cytosolic localization. For many ligands, mutual information between early and late dynamics is low (<20%) suggesting that the two temporal phases can carry distinct information.

Different growth factors induce Akt and ERK to different degrees (Niepel et al., 2014) and this correlates well with the degree of phosphorylation of FoxO3 on Akt and ERK-dependent sites and the extent to which a ligand provokes the two phases of FoxO3 dynamics. For example, IGF1 signals strongly through Akt and primarily induces a harmonic in the principal component decomposition of FoxO3 trajectories that remains high for an extended period of time, whereas BTC signaling is biased toward ERK rather than Akt and primarily induces a harmonic that peaks at t=15 minutes and then falls back to

baseline. Because individual target genes can respond preferentially to constant or oscillatory patterns of transcription factor activity (Purvis et al., 2012; Tay et al., 2010), we speculate that FoxO3 dynamics are read out at the level of target genes involved in cell death, cell cycle progression, ROS detoxification etc. (Jensen et al., 2011; Purvis et al., 2012; Tay et al., 2010). However, our data do not address how this might be achieved; in well-characterized systems such as p53, kinetically related genes do not fall neatly into clusters of similar function (Porter et al., 2016).

Pulsatile regulation of transcription factors is often described as oscillatory, but in the case of FoxO3, spectral density analysis does not reveal a dominant frequency, a key characteristic of a conventional oscillator. Thus FoxO3 does not exhibit either AM or FM encoding (Levine et al., 2013). Instead, we observe a $1/f$ spectrum (where f is frequency), a common characteristic of multi-scale dynamical systems. In F3aN400-Venus trajectories, the $1/f$ power spectrum (also known as pink noise) is convolved by a relatively weak but statistically significant periodic signal with a wavelength of 80 ± 30 minutes (~0.2 mHz), considerably faster than the oscillations of p53 (which have a periodicity of 3–5 hours) (Purvis et al., 2012) but similar to NF-kB (periodicity ~1.5 hr) (Kellogg and Tay, 2015). The origins of $1/f$ and periodic components of FoxO3 trajectories remain unknown.

Combinatorial control over FoxO3 activity

The relationship between FoxO3 pulsing and Akt or ERK activity is complex and non-monotonic. For example, in two cell lines we studied in detail, the highest pulse scores for EGF are observed when ligand concentrations are sub-saturating or ERK is partially inhibited. This effect may be indirect, as the Akt and ERK kinase cascades are known to have multiple mechanisms of cross-regulation, involving both ERK-dependent inhibition of Akt (Yu et al., 2002) and PI3K/Akt-dependent inhibition or stimulation of ERK (Moelling et al., 2002). Our data suggest that ERK regulation of FoxO3 kinetics is at least partly indirect, perhaps via modulation of Akt activity. However, the strength of such cross-talk (as measured by the effect of Akt inhibition on ERK activity and vice-versa) varies with cell line and with ligand. Moreover, whereas our experiments artificially vary FoxO3 dynamics over a range of states using ligands and ERK and Akt inhibitors in combination we speculate that this is achieved physiologically by the combined activities of multiple activating and inhibitory signal transduction cascades.

In tumor cells carrying mutations in ERK and Akt signaling proteins, such as the p85 subunit of PI3K (PIK3CA), HRAS, PTEN phosphatase etc., the range of dynamical states that can be accessed for FoxO3 in response to growth factors is lower (often much lower) than in non-transformed epithelial cells. In some cell types (BT20 for example) FoxO3 is chronically localized in the cytosol and growth factors have little or no effect. In HCC1806 or SKBR3 cells multiple ligands can promote cytosolic translocation, but the range of dynamical states is less than in normal epithelial cells. This suggests that FoxO3 trajectories encode less information in cancer than normal cells. However, more complete understanding of the effects of oncogenic mutations on FoxO3 will require dynamical data from both transformed and non-transformed cell types rather than the fixed cell imaging used to compare tumor cells in the current study.

Conclusion

In the past few years it has been shown that multiple transcription factors and signal transduction kinases alternate between active and inactive states on time scales of minutes to hours. It has been suggested that such systems can encoded information via variation in amplitude (AM encoding) or frequency (FM encoding). FoxO3 dynamics do not conform to either of these possibilities but instead involve independently regulated early and late phases. Late-phase pulsing by FoxO3 is non-oscillatory and synchronous with ERK pulsing, which has been proposed to originate from the stochastic release of autocrine factors among adjacent cells (Sparta et al., 2015). Alternatively, FoxO3 might be regulated by an excitable intracellular feedback circuit subject to stochastic fluctuation (although a pure oscillator degraded by Poisson noise is not expected to have a *1/f* power spectrum) or a chaotic feedback oscillator (Novak and Tyson, 2008). Regardless, multi-part dynamical trajectories represent a potential mechanism for combinatorial control over transcription. It will be interesting to determine whether other transcription factors, including other members of the FoxO family, also have multi-part dynamical trajectories controlled by ligand identity.

STAR METHODS

CONTACT FOR REAGENT AND RESOURCE SHARING

Further information and requests for resources and reagents should be directed to and will be fulfilled by the Lead Contact, Peter Sorger (peter sorger@hms.harvard.edu).

EXPERIMENTAL MODEL AND SUBJECT DETAILS

Tissue culture cell lines—The different cell lines were obtained from the following sources: 184A1 were a gift from the Lauffenburger lab; MCF10A (ATCC® CRL-10317) from ATCC; HCC1806(ATCC® CRL-2335) from ATCC; BT-20 (ATCC® HTB-19) from ATCC; MDA-MB-231 (ATCC® HTB-26) from ATCC; T47D (ATCC® HTB-133) from ATCC; Hs578T (ATCC® HTB-126) from ATCC; MCF7 (ATCC® HTB-22) from ATCC; SKBR3 (ATCC® HTB-30) from ATCC. All cells are quarantined before they are used for experiments and are tested for mycoplasma and other microbial contamination. All cell lines were authenticated by profiling highly- polymorphic short tandem repeat loci (STRs) by the Dana Farber Cancer Institute (DFCI) Molecular Diagnostics Laboratory. The sex of the cell lines are as follows; Female:184A1, MCF10A, HCC1806, BT-20, MDA-MB-231, T47D, Hs578T, MCF7, SKBR3. MCF-10A and 184A1 cells were cultured at 37°C with 5% CO2 in DMEM/F12 (Invitrogen) supplemented with 5% horse serum, 20 ng/mL EGF, 10 μg/mL insulin, 0.5 μg/mL hydrocortisone, 100 ng/mL cholera toxin, 50 U/mL penicillin and 50 μg/mL streptomycin; all other cells were grown according to ATCC recommendations.

METHOD DETAILS

Tissue culture—For experiments involving growth factor stimulation cells were plated and cultured in full growth media for 24 hours. At time of experiment, cells were washed twice with PBS and then placed in serum-free medium (DMEM/F12 with Penicillin/ Streptomycin but no phenol red) for 5 hr, followed by washing and replenishing in fresh serum-free medium for 1hr. Cells were then exposed to growth-factors in serum-free

medium, resulting in a ~5% volume increase. In experiments with kinase inhibitors, drugs were added 1 hr prior to growth factors, unless indicated otherwise.

Construction of plasmids and reporter cell line establishment—The complete coding sequence of human FoxO3 was inserted into pBabe-puro upstream of mVenus and an H212R mutation introduced into the DNA binding domain (Tran et al., 2002). When transduced into MCF10A cells with retroviruses, this construct translocated into the cytosol upon insulin treatment. However, expression levels were uneven among clonal cell populations and cells grew poorly. Thus, a region of FoxO3-H212R corresponding to amino acid residues 1–400 was inserted into pMSCV-puro, upstream of a Venus sequence, to generate pMSCV-puro-F3aN400-Venus. When introduced stably into MCF-10A cells by retroviral transduction, this construct displayed translocation from the nucleus to the cytosol upon insulin treatment, and translocation to the nucleus in response to inhibitors of AKT or PI3K.

To clone fluorescently tagged FoxO3 constructs containing mutations at known sites of phosphorylation a pUC57 plasmid was designed and synthesized by GENEWIZ (Figure S8A), containing an ERK-silent F3aN400- FLAG-mCerulean (with S294A/S344A mutations in FoxO3 sequences), an AKT-silent F3aN400-HA-Venus (with T32A/S253A/S315A in FoxO3) sequences and an NLS-Myc-mCherry, separated by self-cleaving P2A sites. Silent mutations were introduced to create unique restriction sites for generating the following constructs: ERK-silent F3aN400-HA-Venus-P2A-NLS-Myc-mCherry (NaeI) (Figure S8B) or AKT-silent F3aN400-HA- Venus-P2A-NLS-Myc-mCherry (XhoI). To create a FoxO3 construct without AKT- or ERK-specific mutations (F3aN400-HA-Venus-P2A-NLS-Myc-mCherry) from this synthetic construct, a PCR fragment from wildtype-FoxO3 was introduced into the NotI/NaeI sites of ERK-silent F3aN400-HA-Venus-P2A-NLS-Myc-mCherry. All FoxO3 constructs were subsequently subcloned into the EcoRI/SalI restrictions sites of pPB-CAG.EBNXN (A. Bradley, Sanger Institute) containing a puromycin selection cassette.

To create the dual reporter construct pPB-CAG-EKAREV-P2A-F3aN400-HA-mCherry containing the ERK reporter EKAREV (Albeck et al., 2013; Komatsu et al., 2011) and a F3aN400-mCherry separated by a self-cleaving P2A site, PCR fragments were generated from pPB-CAG-EKAREV using the EKAREV primer pairs, pPB-CAG-F3aN400-HA-Venus-P2A-NLS-Myc-mCherry using the F3aN400 primer pairs and pcDNA3-H2B-mCherry, Addgene plasmid 20972 (Nam and Benezra, 2009) using the mCherry primer pairs (Key Resources Table) were cloned into the EcoRI/SalI restriction sites of pPB-CAG-EKAREV using Gibson Assembly (New England BioLabs).

To create stable cell lines and minimize recombination between highly similar fluorescent protein sequences, piggyBac transposon-mediated gene transfer was used; the pPB-CAG expression vectors were co-transfected with a pCMV-hyPBase transposase vector (A. Bradley, Sanger Institute). All FoxO3 sensors were co-expressed with the nuclear reporter NLS-mCherry to facilitate image segmentation, either by double delivery using retroviral infection or by joining the nuclear reporter with the FoxO3 sensor using the P2A ribosomal skipping sequence.

Analysis of total cellular lysates—Cells grown and starved as described above were lysed using RIPA-Buffer (Sigma) supplemented with Complete Protease Inhibitor Cocktail (Roche) with sonication on ice. Extracts were analyzed using SDS-Page followed by transfer to PVDF membranes (Millipore), blocking with Odyssey Blocking Buffer (LI-COR) for 1h, washing with PBS/0.1% Tween and incubation with primary antibody overnight at 4°C in Odyssey Blocking Buffer. Blots were developed and scanned following the Odyssey protocol (LI-COR).

Fixed and live-cell microscopy—For live time-lapse microscopy, cells expressing reporter constructs were plated in 96-well plates at ~ 6×10^5 cells/cm^2 and then imaged using a 10× objective on a Nikon Eclipse inverted fluorescence microscope fitted with an environmental chamber maintained at 37°C with 5% CO_2. Images were collected at 5–10 minutes intervals for a period of 24 hr using the Hamamatsu ORCA-ER cooled CCD camera and Spectra-X light engine (Lumencor). Filter sets used in this study included the polychroic mirror (251050, Chroma), CFP (Ex:440/20, Em:475/20), FRET (Ex:440/20, Em:540/21), YFP (Ex:508/24, Em:540/21) and RFP (Ex:575/22, Em:632/60).

For fixed cell assays for immunostaining, cells were fixed for 10 minutes at room temperature with 2% paraformaldehyde in PBS and then permeabilized with 100% methanol for 10 minutes. After blocking with Odyssey blocking buffer (LI-COR) for 1 hour, cells were incubated with primary antibodies overnight at 4°C. Samples were washed, stained with secondary antibodies at room temperature for 1 hour and counter-stained with DAPI and a whole cell stain (Thermo Scientific) at room temperature for 1 hour. After washing, plates were imaged at 10X using an Operetta high-content imaging system (Perkin Elmer).

QUANTIFICATION AND STATISTICAL ANALYSIS

Calculation of FoxO3 translocation activity—For fixed immunostained cells, image segmentation was performed using cellProfiler (Kamentsky et al., 2011) and extracted features analyzed using MATLAB scripts. For live imaging, cell tracking and segmentation were performed using MATLAB scripts. Image segmentation was performed on the nuclear image of each field using NLS-mCherry signal. Cell tracking was performed by cross-correlation between adjacent frames and validated manually. To calculate FoxO3 translocation dynamics, we first identified nuclear compartment of each cell using either DAPI staining of fixed cells or the NLS-mCherry channel for live microscopy. We then determined the cell boundary either by thresholding to detect the outer cell boundary or by expanding 4 pixels from the nuclear boundary (Figure S1A). We quantified FoxO3 translocation by calculating the ratio between the mean pixel intensity in the cytosolic and nuclear compartments (C/N). For fixed cell studies, FoxO3 intensity was determined by immunostaining cell with anti-FoxO3 antibody. For live microscopy, FoxO3 intensity was derived from direct imaging of the F3aN400 reporter. We often report FoxO3 C/N ratios as log base 10 transformed values (log10(C/N)) so that trajectories with equal FoxO3 intensity inside the nuclear and the cytosolic compartments are centered at 0. To minimize variability in background fluorescence arising from variation in light source or camera drift over time, we first subtracted the mean pixel values in each compartment by the mean pixel value of the background, followed by calculating the log base 10 ratios; this gives rise to the

normalized ratio logio(C_{norm}/N_{norm}) (Figure S1A). For EKAREV, the background signal was first subtracted, and the FRET/CFP ratio calculated at the single pixel level. ERK activity was then calculated from the mean value from the cytosolic compartment of the normalized FRET/CFP values.

Scaling of Western Blots; Error propagation; Total least squares—Protein concentrations were estimated using Western blotting; each measurement (e.g. $pAkt^{S473}$ intensity from blotting) was normalized to its maximum value across an entire experiment. To account for systematic variation within each gel, the intensity of actin staining was used as a calibration standard (Schilling et al., 2005). The following computational analysis was performed to obtain a merged data set. For Immunoblotting, measurement noise is usually log-normal distributed (Kreutz et al., 2007) hence data was log-transformed.

Observations from multiple experiments were merged by assigning each data-point $y_{\text{obs}}(c_{ij}, t_{ik})$ for condition c_{ij} and timepoint t_{ik} a common scaling factor $\hat{s}_i$ for each observable and experiment, i.e. $\hat{y}_{ijk} = \hat{s}_i \cdot y_{\text{obs}}(c_{ij}, t_{ik})$, or

$$y_{ijk} = s_i + log_2\left(y_{\text{obs}}\left(c_{ij}, t_{ik}\right)\right) \quad (1)$$

in the log space. Different gels performed within a single experiment were assumed to be comparable and therefore assigned the same scaling factors. For N experiments, there are $N-1$ degrees of freedom in terms of scaling; therefore, s_1 was set to 1 without loss of generality. To merge data-sets from multiple experiments, the objective function

$$RSS_1 = \sum_{i,j,k} \left(y_m\left(c_j, t_k\right) - y_{ijk}\right)^2 \quad (2)$$

was minimized, yielding the maximum likelihood estimates

$$\left(s_i^*, y^*\left(c_j, t_k\right)\right) = \underset{i}{\text{argmin}}\, RSS_1 \quad (3)$$

for scaling factors s_i^* and merged values $y^*(c_j, t_k)$). For numerical optimization of RSS_1, the MATLAB function *lsqnonlin* was applied using the trust-region method (Coleman and Li, 1996). Using the Jacobian matrix J, we then calculated the uncertainty of estimates from

$$\sigma = \sqrt{\text{diag}\left((J^\dagger J)^{-1}\right)}. \quad (4)$$

Ratios (or differences in log-space) of the merged values

$$r_{jlk} = y^*\left(c_j, t_k\right) - y^*\left(c_l, t_k\right) \quad (5)$$

were calculated as final readout of the analysis. Uncertainties were propagated using the following equation:

$$\sigma\left(r_{jlk}\right) = \sqrt{\sigma(y^*(c_j, t_k))^2 + (\sigma(y^*(c_l, t_k))^2}\,. \quad (6)$$

Eq. 6 was used to determine propagated errors for the pERK/pAKT ratios in Fig. 1C. For any indexed sets M = $\{jlk_1, jlk_2, jlk_M\}$ and Q = $\{opq_1, opq_2, \cdot, opq_M\}$ with samples that share a linear relationship, we assume a linear model $ax + b$ for the relationshipof (r_M, r_Q), and can apply total least squares to determine estimates and uncertainties of both dependent and independent variables simultaneously. For this purpose, the following objective function

$$RSS_2 = \sum_{\mathrm{M\,Q}} \frac{1}{\sigma\left(r_{jkl}\right)}\left(r_{jkl} - \frac{r_{opq} - b}{a}\right) + \frac{1}{\sigma\left(r_{opq}\right)}\left(r_{opq} - a \cdot r_{opq} - b\right) \quad (7)$$

was numerically optimized as disscussed in Eq. (3). Using this formula, the constraint of relative data having an unknown scaling factor with respect to concentration level does not influence the slope *a*, but only offseting *b*. Different experiments are scaled in reference with each other, resulting in merged y* and corresponding uncertainties. Ratios of normalized parameters were then calculated. In our study (Figure 1C), we applied this approaches to the ratios of pERK/pAKT and pS294/pS253, and a linear model was fitted to their relationship using total least squares.

Functional principal component analysis (fPCA)—To analyze the underlying trends of the reporter translocation trajectories, we implemented functional principal component analysis (fPCA). Similar to classical principal component analysis, this technique generates an empirical set of orthogonal basis functions $\psi_i(t)$ that comply with

$$\left\langle \psi_i, \psi_j \right\rangle = \int \psi_i(t)\psi_j(t)dt = 0 \quad (8)$$

and these basis functions also yield maximal variance for any $i \neq j$. We first applied this technique for the early synchronous response, with $t \in$ [—70,80] min. Equidistantly spaced cubic b-splines (De Boor, 2001) were used to convert the input signals to continuous time-courses. We smoothed the signals using 1.5 data-points per basis function to avoid overfitting. Artifacts at the edges, normally arising at the beginning and at the end of each trajectory, were not an issue here because of the high number of trajectories for basis calculation (total of over 5000 trajectories). Using the implementation described by Ramsay (Ramsay et al., 2009; Ramsay and Silverman, 2005), we identified three orthonormal basis

functions (harmonics) that together explain over 95% of the observed variance. To make biologial senses of the observed basis functions, we rotated the three basis functions using the following transformation:

$$R = \begin{pmatrix} 1 & 0 & 0 \\ 0 & \cos\theta_3 & \sin\theta_3 \\ 0 & -\sin\theta_3 & \cos\theta_3 \end{pmatrix} \begin{pmatrix} \cos\theta_2 & 0 & -\sin\theta_2 \\ 0 & 1 & 0 \\ \sin\theta_2 & 0 & \cos\theta_2 \end{pmatrix} \begin{pmatrix} \cos\theta_1 & \sin\theta_1 & 0 \\ -\sin\theta_1 & \cos\theta_1 & 0 \\ 0 & 0 & 1 \end{pmatrix} \quad (9)$$

using Euler angles $\theta_1 = -25°$, $\theta_2 = 5°$ and $\theta_3 = -5°$. The first harmonic, fPC1 corresponds to a steady-state value prior to ligand addition and is not significantly different between growth factor stimuli (Figure 3C). The second harmonic fPC2 corresponds to a sustained translocation starting at t=0 min and the third harmonic fPC3 corresponds to a transient function that falls below baseline at t=60 min. For t > 80 min, all harmonics converge to the Fourier basis, implying that trajectories from late-response are truely asynchronous.

Pulse score and fraction ofpulsing cells—Trajectories artifacts such as spikes resulting from cell division or loss of cell tracking were first removed by interpolation. Missing values were added by interpolation for fPCA and dropped in subsequent analysis. For F3aN400-Venus translocation trajectories, the first three fPCA harmonics were employed to detrend the signals (as shown in Figure 4A) and an additive model of slow trend and fast pulsing assumed. The detrended signal was smoothed using $N/3$ bsplines for N data points. For EKAREV traces, an averaged trend determined from average sliding window was first applied to detrend the signal. Peaks were then detected on smoothed and detrended trajectories. Due to overfitting, pulsatile traces often contain small peaks. We dropped small peaks with edge height less than 0.005. The final detrended, interpolated, and peak adjusted signals were used for detecting edges that connect from peak to peak of each trajectory. As a result, we can define edges into two finite sets: $T_{\text{start}} = \{t_{s(1)},\ldots,t_{s(N_{\text{edge}})}\}$ and $T_{\text{end}} = \{t_{e(1)},\ldots, t_{e(N_{\text{edge}})}\}$, depicting the starting and ending points of all edges, respectively. The index set $I \subset \{1,\ldots, N_{\text{edge}}\}$ with N_I elements contains indices of edges that are directly connected to a neighboring edge. Superscripts + and - denote ascending and descending edges and $N_{\text{peak}}$the total number of peaks. The deviation of the smoothed signal y and data y^D is quantified with $RSS = \sum_{k=1}^{N} \left(y(t_k) - y^D(t_k)\right)^2$.

For calculating the pulse score, the following features f_i were extracted (See also Figure 4B)

1. Number of pulse edges: $f_1 = N_{edge} \approx 2N_{\text{peak}}$
2. Pulse amplitude: $f_2 = \max\tilde{y}(t) - \min\tilde{y}(t)$
3. Signal to noise ratio: $f_3 = \frac{f_2}{1/(N-1)\sqrt{RSS}}$
4. Peak duration: $f_4 = \frac{1}{N_{\text{I}}}\sum_{i \in \text{I}} \left|t_{s(i)} - t_{e(i+1)}\right|$

5. Peak distance:

$$f_5 = \frac{1}{N_{\text{edge}}-1}\sum_{i=1}^{N_{\text{edge}}-1}\left|t^{\pm}_{s(i+1)} - t^{\pm}_{s(i)}\right| + \frac{1}{N_{\text{edge}}-1}\sum_{i=1}^{N_{\text{edge}}-1}\left|t^{\pm}_{e(i+1)} - t^{\pm}_{e(i)}\right|$$

Whenever no peaks were detected, peak duration and peak distance were set to 300 min. A reference value r_i and a set of weights w_i was defined for all features f_i. Positive values for w_i represent features for which a larger value corresponds to more pulsing, i.e. number of edges, amplitude, and signal to noise ratio. Respectively, a negative number for w_i depicts a feature for which a larger value indicates less pulsing, namely peak duration and peak distance. Using the features f_i, the reference values r_i, and the weights w_i, the pulsatory score was calculated for each trajectory based on the following formula:

$$p = \prod_i \left(\frac{f_i}{r_i}\right)^{w_i}. \quad (10)$$

Reference values and weights were adjusted by sorting trajectories by their pulse score p to achieve visual ordering of pulsing. Resulted reference values and weights are r = (90, 0.04, 40, 300, 300) and w = (2, 1, 1.5, - 1.5, −1.5), for all five characteristics of pulse score, respectively. A threshold pulse score of 0.6 was used for assigning each trajectory into the pulsing or non-pulsing groups. The choice of 0.6 was supported by visual inspection that this threshold can best separate BTC-stimulated cells from IGFl-stimulated condition (Figure 4A). Finally, the fraction of pulsing cells was calculated for each condition based on

$$\text{fp} = \frac{N_{\text{pulsing}}}{N_{\text{all}}}. \quad (11)$$

Power spectrum analysis—Time-course measurements from single cells were ordered according to their pulsatory score and subsequently grouped based on their percentile ranking into 4 bins: <10$^{\text{th}}$, 25$^{\text{th}}$-50$^{\text{th}}$, 50$^{\text{th}}$-75$^{\text{th}}$ and >90$^{\text{th}}$. For each trace $y(t_n)$ the corresponding periodogram

$$|Y(f)|^2 = \frac{\Delta t}{N}\cdot\left|\sum_{n=1}^{N} y(t_n)e^{-ifn}\right|^2 \quad (12)$$

was calculated. To minimize leakage effects due to the finite time-window of observation, signals were tapered using a triangular window. The power spectrum was finally calculated by averaging periodograms from all traces in each bin. Spectra of simulated time-courses were also included as references, namely 1) pink noise (Bak et al., 1987) and 2) white noise added to a sinusoidal wave

$$y_{\sin}(t_n) = s_1 \sin\left(2\pi t_n / r_f\right) + s_2 e \quad (13)$$

using an independent and identically distributed random variable $e \in N(0,1)$, weighting factors s_i to adjust the scales, and the reference frequency r_f of 80 min.

Mutual information—To assess the predictability of pulsing classification from the early PC scores, we applied the concept of mutual information (MI). Specifically, the MIxnyn implementation of the MILCA algorithm (Kraskov et al., 2004) was used to determine the MI score between the discretized pulse score (0 = non-pulsing; 1 = pulsing) and the corresponding early fPC scores for each trajectory. MI scores were determined for individual fPC score as well as for combined fPC scores. As reference, we used the entropy of pulsing classification H(fp) = MI(fp,fp). *Fixed-cell analysis of ERK-AKT-FoxO3 connectivity*

Data of phosphorylated ERK-T202/Y204 or AKT-S473 and the nuclear translocation of FoxO were collected in 9 cell lines (MCF10A, 184A1, HS578T, BT20, SKBR3, MDA231, MCF7, HCC1806, and T47D) at 8 time points. Several perturbation conditions were measured consisting of stimulation with one of 7 growth factors and no treatment control (8 ligand options), with or without AKT and/or MEK inhibitors (4 inhibitor conditions). This results in a total of 32 perturbation conditions.

Because the activity of endogenous FoxO3 was obtained from different cell populations at different time points, it was not possible to learn a dynamical model directly using measurement at single-cell resolution. We therefore chose quantities representing the characteristics of the population distribution of each measured signal. For the measurement of pERK and pAKT, we chose to use their medians (ERK μ, AKT μ) as measures of the net level of signal activation at the cell population level. These values were normalized by their maximal values on a per-cell line basis. For FoxO3, we found that perturbations affect both the position (median) and the spreading (inter-quartile range, IQR) of the C/N ratio. We therefore used positions along the curve of FoxO3 C/N translocation ratios in the median vs. IQR landscapes (Figure 7B) as the representative value of FoxO3 activity. In what follows, we will denote this value by FoxO3 $\varnothing$. With this approach we expect to show a dependence of FoxO3 on ERK and AKT both in terms of its level and its variability (see Figure S9A).

Quantifying ERK, AKT and FoxO3 response to inhibitors—To quantify the effect of MEK inhibition on AKT phosphorylation, we calculated the difference in the median values for AKT, AKT μ, at each time point (separately for each combination of cell line and growth factor), in two different inhibitor conditions: with the MEK inhibitor pre-treatment and without any inhibitor pretreatment (DMSO). This resulted in a vector of difference values across the 8 time points, which we deduced using the corresponding area under the curve. This gives a lumped measure of the overall effect of MEK inhibition on AKT phosphorylation for each cell line/growth factor pair (Figure 7C). To further summarize this effect across all ligand conditions, we took the mean of the AUC values across all ligands to obtain a single representative value for each cell line (red crosses in Figure 7E). Quantification on the effect of AKT inhibition on ERK phosphorylation (ERK μ) was also done in the same manner (Figure 7D and black crosses in Figure 7E).

To quantify the effect on FoxO3 by either MEK or AKT inhibition, we used the same AUC-based method but on the position along the parabola in the median vs. IQR landscape (FoxO3 ∅), as described above.

Approach to Bayesian model comparison—We used the above fixed-cell data from various cell lines to perform Bayesian model discrimination in comparing hypotheses that can best describe the contribution of ERK and AKT activity in FoxO3 translocation. We applied three different dynamic Bayesian network scoring schemes to compare these model hypotheses: two based on a conditionally Gaussian probabilistic model and the third using a discretized approach. From the Bayesian scores obtained from each model we derive probabilities for the support for each individual causal edge between ERK, AKT and FoxO3.

When using the Gaussian-based scoring schemes, we directly used the values described above. For the scoring scheme relying on discrete data, we first performed data discretization as follows. We took data points for each of the 3 variables and independently applied Otsu's discretization technique (Otsu, 1979), which calculates for the optimum threshold such that the intra-class variance is minimized between two groups to which the values are discretized.

Comparing model topologies—We were interested in evaluating causal dependencies representing the relationships between ERK, AKT and FoxO3. We considered four relationships of interest:

1. AKT controlling FoxO3 independent of ERK
2. ERK controlling FoxO3 independent of AKT
3. ERK controlling AKT
4. AKT controlling ERK.

These mechanisms are represented as edges shown in Figure S9B.

We translated these model hypotheses into probabilistic model structures and used Bayesian scoring schemes to quantitatively assess the plausibility of each hypothesis with respect to experimental data. Since there are a total of 4 allowed edges in each model, there are a total of $2^4 = 16$ possible overall topologies to consider.

Given a data set D and a set of model topologies M_k, $1 \le k \le 16$, we first calculate the posterior probability of each model,

$$P(M_k|D) = \frac{P(D|M_k)P(M_k)}{P(D)}. \quad (14)$$

Here $P(D \mid M_k)$ is the *marginal likelihood* of model M_k, and $P(M_k)$ is the prior probability assigned to the model. We assign equal prior probability to all four models, that is, $P(M_1) = P(M_2) = P(M_3) = P(M_4)$. Consequently, we can calculate the posterior odds of two models as:

$$\frac{P(M_k|D)}{P(M_j|D)} = \frac{P(D|M_k)P(M_k)}{P(D|M_j)P(M_j)} = \frac{P(D|M_k)}{P(D|M_j)}, \quad 1 \le j \ne k \le 4. \quad (15)$$

This shows that models can be compared through their marginal likelihoods. We now turn to the methods for calculation of the marginal likelihood for each model hypothesis. Calculating the marginal likelihood depends on the type of probabilistic model and the assumed parametrization. For model parameters M_k summarized in a vector θ_k, the marginal likelihood is expressed as

$$P(D|M_k) = \int P(D|M_k, \theta_k)P(\theta_k|M_k)d\theta_k . \quad (16)$$

A score is thereby assigned to a model by integrating over all possible parametrizations. In many cases the parametrization of the model is such that this integral can be solved analytically (we will consider three such methods), in other cases numerical methods can be used to calculate it. For a general introduction to learning Bayesian networks, we refer the reader to (Neapolitan, 2004).

Computing dynamic Bayesian networks—Assume a network on a set of n variables $X = \{X_1,..., X_n\}$. The edges representing the model structure can then be described through the parenthood relationship $Pa : X \rightarrow 2^X$. Namely, an edge exists from X_i to X_j if and only if $X_i \in Pa(X_j)$, with $1 \le i, j \le n$. The model is parameterized through a set of conditional probability distributions specifying the distribution of a variable given the value of its parents, or $P(X_i \mid Pa(X_i))$. Through this parenthood relationship, the joint distribution can be written as

$$P(X_1, \ldots, X_n) = \prod_{i=1}^{n} P(X_i|Pa(X_i)) . \quad (17)$$

The above equation shows that the joint distribution of the variables can be derived from the local parenthood structure of each node.

Dynamic Bayesian networks are a special case of Bayesian networks and are used to represent a set of random variables across multiple time points (Murphy, 2002). There are at least two important advantages of using a dynamic Bayesian network compared to static Bayesian network in our setting. First, DBNs allow us to use the available time resolved experimental data directly to learn the model. Second, due to the fact that DBN edges point forward in time, it is possible to model feedback effects (that would normally result in disallowed loops in Bayesian network graphs). Assuming there are a total of T time points of interest in the process, a DBN will consist of a node representing each of n variables at each of the T time points. For instance X_i^t will denote the i-th variable at time point t. Per the

standard assumption in the context of DBNs, we assume that the each variable at time t is independent of all previous variables given the value of its parent variables at time t — 1. Hence the edges in the network point forward in time and only span a single time step.

We represented as variables the median (μ) of the single-cell measured values of phosphorylated ERK and AKT and the position along the median vs. IQR landscape (ϕ) of FoxO3 activity at each experimental time point, yielding three random variables. We represented each random variable at each time point where experimental data was available, resulting in a network with a total of 24 random variables. We assume that the structure of the network does not change over time and also that the parameterization is time-invariant. This allows us to use all data for pairs of subsequent time points to score models. Figure S9C shows the DBN representation of one model topology (the topology with all possible edges present). Assuming that the prior probability of each model topology is equal, from these marginal likelihood values, we can calculate the marginal probability of a specific edge e being present as follows

$$P(e) = \frac{\sum_i \left[P\left(M_i \middle| D\right) \middle| e \in M_i\right]}{\sum_i P\left(M_i \middle| D\right)}. \quad (18)$$

We applied three different approaches to scoring DBN models and thereby obtaining individual edge probabilities.

DBN learning with the BGe score—In the BGe scoring approach (results shown in Figure S7C) (Geiger and Heckerman, 1994; Grzegorczyk, 2010) data is assumed to be generated from a conditionally Gaussian distribution with a normal-Wishart prior distribution on the model parameters. The observation is assumed to be distributed as $N(\mu, \Sigma)$ with the conditional distribution of μ defined as $N(\mu_0, (\nu W)^{-1})$ and the marginal distribution of W as $W(\alpha, T_0)$, that is, a Wishart distribution with α degrees of freedom and T_0 covariance matrix. We define the hyperparameters of the priors as follows. We set

$$\nu := 1, \quad \alpha := n + 2$$

$$\mu_{0,j} := 0, \quad 1 \le j \le n,$$

$$T_0 := \frac{\nu(\alpha - n - 1)}{\nu + 1} I_{n,n},$$

where n is the total number of modeled species. The marginal likelihood of a model for a subset of the data D' on n' nodes with these assumptions can be expressed as follows.

$$P\left(D' \middle| M_k\right) = (2\pi)^{-n'm/2} \cdot \left(\frac{\nu}{\nu + m}\right)^{n'/2} \cdot \frac{c(n', \alpha)}{c(n', \alpha + m)} \cdot \det\left(T_0\right)^{\alpha/2} \cdot \det\left(T_{D',m}\right)^{-(\alpha + m)/2}, \quad (19)$$

With

$$T_{D,m} = D_0 + (m-1)\cdot Cov(D) + \frac{\nu m}{\nu + m}(\mu_0 - \bar{D})(\mu_0 - \bar{D})^T, \quad (20)$$

and

$$c(n,\alpha) = \left(2^{\alpha n/2}\cdot \pi^{n(n-1)/4}\prod_{i=1}^{n}\Gamma\left(\frac{\alpha+1-i}{2}\right)\right)^{-1}. \quad (21)$$

The full marginal likelihood is then calculated as

$$P(D|M_k) = \prod_{i=1}^{n}\frac{P\left(D^{i,\pi_i}\middle|M_k\right)}{P\left(D^{\pi_i}\middle|M_k\right)}, \quad (22)$$

where D^{i,π_i} denotes the subset of the data for the i-th node and its parents and D^{π_i} the subset of data for the i-th node's parents only. Note that these subsets of data are constructed such that the data for the i-th node is shifted forward by one time-step to align with the parents' data.

DBN learning with g-prior based Gaussian score—We adapted the DBN learning approach developed by Hill et al. (results shown in Figure 7F) (Hill et al., 2012). This approach is similar to the BGe approach in that it assumes a conditional Gaussian probability distribution for the variables in the model. It, however, chooses a different prior parametrization leading to desirable properties including the fact that parameters don't need to be user-set and that the score is invariant to data rescaling. One shortcoming of this method is that it requires matrix inversion and is therefore prone to conditioning problems, Here we only present the formula for the marginal likelihood calculation and refer to Hill et al. (2012) for the details of the conditional probability model. The formula for calculating the marginal likelihood for node i is

$$P\left(D_i\middle|M_k\right) = (1+m)^{-(2^{|\pi_i|}-1)/2}\left(D_i^T D_i - \frac{m}{m+1}D_i^T B_i\left(B_i^T B_i\right)^{-1}B_i^T D_i\right)^{-m/2}, \quad (23)$$

where D_t is the subset of the data for the i-th variable, shifted forward by one time step, B_i is a design matrix containing the data for the i-th node's parents and possibly the higher order products of the parents' data to model upstream interactions. We do not use higher order interaction terms in the current study. The full marginal likelihood is expressed as

$$P(D \mid M_k) = \prod_{i=1}^{n} P(D_i \mid M_k). \quad (24)$$

DBN learning with the BDe score—The BDe scoring metric (results shown in Figure S7D) (Friedman et al., 1998; Heckerman et al., 1995a) relies on the assumption that each random variable is binary, that is, $X_t \in \{0,1\}$. Consequently, the model is parametrized by a set of conditional probability tables containing the probabilities that a node takes the value 1 given all possible combinations of values assigned to its parents. For instance, in a specific topology, the conditional probability table of FoxO3 ϕ could consist of the entries $P(\text{FoxO3a}\phi^t = v_1 \mid \text{AKT}\mu^{t-1} = v_2)$ for all combinations of $v_1, v_2 \in \{0,1\}$. Note that the conditional probability distributions have to sum to one, that is, $\sum_{v_1 \in \{0,1\}} P(\text{Foxo3a}\phi^t = v_1 \mid \text{AKT}\mu^t = v_2) = 1$.

The BDe score assumes a beta distribution as the prior for the model parameters. Using beta priors, Heckerman et al. (1995 a) shows that the marginal likelihood can be expressed as

$$P(D \mid M_k) = \prod_{i=1}^{n} \prod_{j=1}^{q_i} \frac{\Gamma(s_{ij})}{\Gamma(d_{ij} + s_{ij})} \prod_{\ell \in \{0,1\}} \frac{\Gamma(d_{ij\ell} + s_{ij\ell})}{\Gamma(s_{ij\ell})}, \quad (25)$$

where i refers to a node X_i, j is a value configuration of the parents of node X_i, with q_i the total number of parent value configurations, and ℓ indicates the value of node X_i under parent configuration j. For each combination of indices, d_{ij} and $d_{ij\ell}$ represent the observed count, while s_{ij} and $s_{ij\ell}$ are the prior counts. To make priors consistent among different DAG structures, we choose a fix equivalent sample size $S = 1$, and set $s_{ij\ell} = S / (2q_i)$. For instance, assume we want to score the model M_1, and that we denote X_3 = AKT μ and X_5 = FoxO3 μ, with which $Pa(X_5) = \{X_3\}$, and $q_5 = 2$. Then, for instance, d_{510} is the number of experiments in which AKT μ takes the value 0 and FoxO3 μ takes the value 0. Similarly, d_{51} corresponds to the number of experiments in which AKT μ takes the value 0.

DATA AND SOFTWARE AVAILABILITY

Raw images and LINCS-compatible CSV datasets can be accessed at http://lincs.hms.harvard.edu/sampattavanich-cellsyst-2018/.

Extracted data in other formats are available at https://doi.org/10.17632/65fkdzt9x5.1.

Scripts used to generate all figures are available at https://github.com/sorgerlab/sampattavanich-cellsvst-2018.

CELL-SYSTEMS-D-16–00201R1

Encoding growth factor identity in the temporal dynamics of FoxO3 under the combinatorial control of ERK and AKT Kinases

Supplementary Material

Refer to Web version on PubMed Central for supplementary material.

ACKNOWLEDGMENTS

This work was funded by 50GM107618 and U54HL127365 to PKS, a “Chalermphrakiat” Grant (Mahidol University) and the Thai Research Fund (TRG5880094) to SS, and the German BMBF (SBEpo 0316182A and 0316042G) to BS. We thank J. Timmer, V. Becker, J. Sims, J. Waters, H. Elliott, the HMS-Nikon and IDAC Core Facilities, K. Aoki for EKAREV plasmid and A Bradley for PiggyBAC.

REFERENCES

Albeck JG, Mills GB, and Brugge JS (2013). Frequency-modulated pulses of ERK activity transmit quantitative proliferation signals. Mol Cell 49, 249–261. [PubMed: 23219535]

Aoki K, Kumagai Y, Sakurai A, Komatsu N, Fujita Y, Shionyu C, and Matsuda M (2013). Stochastic ERK activation induced by noise and cell-to-cell propagation regulates cell density-dependent proliferation. Mol Cell 52, 529–540. [PubMed: 24140422]

Bak P, Tang C, and Wiesenfeld K (1987). Self-organized criticality: An explanation of the 1/f noise. Phys Rev Lett 59, 381–384. [PubMed: 10035754]

Batchelor E, Loewer A, Mock C, and Lahav G (2011). Stimulus-dependent dynamics of p53 in single cells. Mol Syst Biol 7, 488. [PubMed: 21556066]

Batchelor E, Mock CS, Bhan I, Loewer A, and Lahav G (2008). Recurrent initiation: a mechanism for triggering p53 pulses in response to DNA damage. Mol Cell 30, 277–289. [PubMed: 18471974]

Biggs WH, 3rd, Meisenhelder J, Hunter T, Cavenee WK, and Arden KC (1999). Protein kinase B/Akt-mediated phosphorylation promotes nuclear exclusion of the winged helix transcription factor FKHR1. Proceedings of the National Academy of Sciences of the United States of America 96, 7421–7426. [PubMed: 10377430]

Brunet A, Bonni A, Zigmond MJ, Lin MZ, Juo P, Hu LS, Anderson MJ, Arden KC, Blenis J, and Greenberg ME (1999). Akt promotes cell survival by phosphorylating and inhibiting a Forkhead transcription factor. Cell 96, 857–868. [PubMed: 10102273]

Brunet A, Kanai F, Stehn J, Xu J, Sarbassova D, Frangioni JV, Dalal SN, DeCaprio JA, Greenberg ME, and Yaffe MB (2002). 14–3-3 transits to the nucleus and participates in dynamic nucleocytoplasmic transport. The Journal of cell biology 156, 817–828. [PubMed: 11864996]

Brunet A, Park J, Tran H, Hu LS, Hemmings BA, and Greenberg ME (2001). Protein kinase SGK mediates survival signals by phosphorylating the forkhead transcription factor FKHRL1 (FOXO3a). Molecular and cellular biology 21, 952–965. [PubMed: 11154281]

Cai L, Dalal CK, and Elowitz MB (2008). Frequency-modulated nuclear localization bursts coordinate gene regulation. Nature 455, 485–490. [PubMed: 18818649]

Calnan DR, and Brunet A (2008). The FoxO code. Oncogene 27, 2276–2288. [PubMed: 18391970]

Chen JY, Lin JR, Cimprich KA, and Meyer T (2012). A two-dimensional ERK-AKT signaling code for an NGF-triggered cell-fate decision. Mol Cell 45, 196–209. [PubMed: 22206868]

Cheong R, Rhee A, Wang CJ, Nemenman I, and Levchenko A (2011). Information transduction capacity of noisy biochemical signaling networks. Science 334, 354–358. [PubMed: 21921160]

Coleman TF, and Li Y (1996). An Interior Trust Region Approach for Nonlinear Minimization Subject to Bounds. SIAM Journal on Optimization 6, 418–445.

De Boor C (2001). A practical guide to splines : with 32 figures, Rev. edn (New York: Springer).

Eijkelenboom A, and Burgering BM (2013). FOXOs: signalling integrators for homeostasis maintenance. Nature reviews Molecular cell biology 14, 83–97. [PubMed: 23325358]

Elowitz MB, and Leibler S (2000). A synthetic oscillatory network of transcriptional regulators. Nature 403, 335–338. [PubMed: 10659856]

Essers MA, Weijzen S, de Vries-Smits AM, Saarloos I, de Ruiter ND, Bos JL, and Burgering BM (2004). FOXO transcription factor activation by oxidative stress mediated by the small GTPase Ral and JNK. EMBO J 23, 4802–4812. [PubMed: 15538382]

Friedman N, Linial M, Nachman I, and Pe'er D (2000). Using Bayesian networks to analyze expression data. J Comput Biol 7, 601–620. [PubMed: 11108481]

Friedman N, Murphy K, and Russell S (1998). Learning the structure of dynamic probabilistic networks In Proceedings of the Fourteenth conference on Uncertainty in artificial intelligence (Madison, Wisconsin: Morgan Kaufmann Publishers Inc), pp. 139–147.

Geiger D, and Heckerman D (1994). Learning Gaussian networks In Proceedings of the Tenth international conference on Uncertainty in artificial intelligence (Seattle, WA: Morgan Kaufmann Publishers Inc), pp. 235–243.

Greer EL, Oskoui PR, Banko MR, Maniar JM, Gygi MP, Gygi SP, and Brunet A (2007). The energy sensor AMP-activated protein kinase directly regulates the mammalian FOXO3 transcription factor. J Biol Chem 282, 30107–30119. [PubMed: 17711846]

Gross SM, and Rotwein P (2015). Akt signaling dynamics in individual cells. J Cell Sci 128, 2509–2519. [PubMed: 26040286]

Grzegorczyk M (2010). An introduction to Gaussian Bayesian networks. Methods Mol Biol 662, 121–147. [PubMed: 20824469]

Halford D, Shoaf JH, and Risley AS (1973). Spectral density analysis: Frequency domain specification and measurement of signal stability. 27th Annual Symposium on Frequency Control, 421–431.

Hansen AS, and O'Shea EK (2015). Limits on information transduction through amplitude and frequency regulation of transcription factor activity. Elife 4.

Hansen AS, and O'Shea EK (2016). Encoding four gene expression programs in the activation dynamics of a single transcription factor. Curr Biol 26, R269–271. [PubMed: 27046808]

Hao N, and O'Shea EK (2011). Signal-dependent dynamics of transcription factor translocation controls gene expression. Nat Struct Mol Biol 19, 31–39. [PubMed: 22179789]

Hausdorff JM, and Peng C (1996). Multiscaled randomness: A possible source of 1/f noise in biology. Phys Rev E Stat Phys Plasmas Fluids Relat Interdiscip Topics 54, 2154–2157. [PubMed: 9965304]

Heckerman D, Geiger D, and Chickering DM (1995a). Learning Bayesian Networks: The Combination of Knowledge and Statistical Data. Machine Learning 20, 197–243.

Heckerman D, Geiger D, and D.M. C (1995b). Learning Bayesian Networks: The Combination of Knowledge and Statistical Data. Machine Learning 20, 197–243.

Hill SM, Lu Y, Molina J, Heiser LM, Spellman PT, Speed TP, Gray JW, Mills GB, and Mukherjee S (2012). Bayesian inference of signaling network topology in a cancer cell line. Bioinformatics 28, 2804–2810. [PubMed: 22923301]

Hu MC, Lee DF, Xia W, Golfman LS, Ou-Yang F, Yang JY, Zou Y, Bao S, Hanada N, Saso H, et al. (2004). IkappaB kinase promotes tumorigenesis through inhibition of forkhead FOXO3a. Cell 117, 225–237. [PubMed: 15084260]

Huang H, Regan KM, Lou Z, Chen J, and Tindall DJ (2006). CDK2-dependent phosphorylation of FOXO1 as an apoptotic response to DNA damage. Science 314, 294–297. [PubMed: 17038621]

Jensen KS, Binderup T, Jensen KT, Therkelsen I, Borup R, Nilsson E, Multhaupt H, Bouchard C, Quistorff B, Kjaer A, et al. (2011). FoxO3A promotes metabolic adaptation to hypoxia by antagonizing Myc function. EMBO J 30, 4554–4570. [PubMed: 21915097]

Kamentsky L, Jones TR, Fraser A, Bray MA, Logan DJ, Madden KL, Ljosa V, Rueden C, Eliceiri KW, and Carpenter AE (2011). Improved structure, function and compatibility for CellProfiler: modular high- throughput image analysis software. Bioinformatics 27, 1179–1180. [PubMed: 21349861]

Kellogg RA, and Tay S (2015). Noise facilitates transcriptional control under dynamic inputs. Cell 160, 381392.

Komatsu N, Aoki K, Yamada M, Yukinaga H, Fujita Y, Kamioka Y, and Matsuda M (2011). Development of an optimized backbone of FRET biosensors for kinases and GTPases. Mol Biol Cell 22, 46474656.

Kraskov A, Stögbauer H, and Grassberger P (2004). Estimating mutual information. Physical Review E 69, 066138.

Kreutz C, Bartolome Rodriguez MM, Maiwald T, Seidl M, Blum HE, Mohr L, and Timmer J (2007). An error model for protein quantification. Bioinformatics 23, 2747–2753. [PubMed: 17768165]

Lahav G, Rosenfeld N, Sigal A, Geva-Zatorsky N, Levine AJ, Elowitz MB, and Alon U (2004). Dynamics of the p53-Mdm2 feedback loop in individual cells. Nat Genet 36, 147–150. [PubMed: 14730303]

Lehtinen MK, Yuan Z, Boag PR, Yang Y, Villen J, Becker EB, DiBacco S, de la Iglesia N, Gygi S, Blackwell TK, et al. (2006). A conserved MST-FOXO signaling pathway mediates oxidative-stress responses and extends life span. Cell 125, 987–1001. [PubMed: 16751106]

Lev Bar-Or R, Maya R, Segel LA, Alon U, Levine AJ, and Oren M (2000). Generation of oscillations by the p53-Mdm2 feedback loop: a theoretical and experimental study. Proceedings of the National Academy of Sciences of the United States of America 97, 11250–11255. [PubMed: 11016968]

Levine JH, Lin Y, and Elowitz MB (2013). Functional roles of pulsing in genetic circuits. Science 342, 1193–1200. [PubMed: 24311681]

Li Z, Kowitsch A, Zhou G, Groth T, Fuhrmann B, Niepel M, Amado E, and Kressler J (2013). Enantiopure chiral poly(glycerol methacrylate) self-assembled monolayers knock down protein adsorption and cell adhesion. Adv Healthc Mater 2, 1377–1387. [PubMed: 23526806]

Lin Y, Sohn CH, Dalal CK, Cai L, and Elowitz MB (2015). Combinatorial gene regulation by modulation of relative pulse timing. Nature 527, 54–58. [PubMed: 26466562]

Moelling K, Schad K, Bosse M, Zimmermann S, and Schweneker M (2002). Regulation of Raf-Akt Crosstalk. J Biol Chem 277, 31099–31106. [PubMed: 12048182]

Murphy KP (2002). Dynamic bayesian networks: representation, inference and learning (University of California, Berkeley), pp. 268.

Nam HS, and Benezra R (2009). High levels of Id1 expression define B1 type adult neural stem cells. Cell Stem Cell 5, 515–526. [PubMed: 19896442]

Neapolitan RE (2004). Learning Bayesian networks (Upper Saddle River, N.J.: Pearson Prentice Hall).

Nelson DE, Ihekwaba AE, Elliott M, Johnson JR, Gibney CA, Foreman BE, Nelson G, See V, Horton CA, Spiller DG, et al. (2004). Oscillations in NF-kappaB signaling control the dynamics of gene expression. Science 306, 704–708. [PubMed: 15499023]

Niepel M, Hafner M, Pace EA, Chung M, Chai DH, Zhou L, Muhlich JL, Schoeberl B, and Sorger PK (2014). Analysis of growth factor signaling in genetically diverse breast cancer lines. BMC Biol 12, 20. [PubMed: 24655548]

Novak B, and Tyson JJ (2008). Design principles of biochemical oscillators. Nat Rev Mol Cell Biol 9, 981991.

Otsu N (1979). A Threshold Selection Method from Gray-Level Histograms. IEEE Transactions on Systems, Man, and Cybernetics 9, 62–66.

Porter JR, Fisher BE, and Batchelor E (2016). p53 Pulses Diversify Target Gene Expression Dynamics in an mRNA Half-Life-Dependent Manner and Delineate Co-regulated Target Gene Subnetworks. Cell Syst 2, 272282.

Purvis JE, Karhohs KW, Mock C, Batchelor E, Loewer A, and Lahav G (2012). p53 dynamics control cell fate. Science 336, 1440–1444. [PubMed: 22700930]

Purvis JE, and Lahav G (2013). Encoding and decoding cellular information through signaling dynamics. Cell 152, 945–956. [PubMed: 23452846]

Ramsay JO, Hooker G, and Graves S (2009). Functional data analysis with R and MATLAB (Dordrecht; New York: Springer).

Ramsay JO, and Silverman BW (2005). Functional data analysis, 2nd edn (New York: Springer).

Schilling M, Maiwald T, Bohl S, Kollmann M, Kreutz C, Timmer J, and Klingmuller U (2005). Computational processing and error reduction strategies for standardized quantitative data in biological networks. FEBS J 272, 6400–6411. [PubMed: 16336276]

Senapedis WT, Kennedy CJ, Boyle PM, and Silver PA (2011). Whole genome siRNA cell-based screen links mitochondria to Akt signaling network through uncoupling of electron transport chain. Mol Biol Cell 22, 1791–1805. [PubMed: 21460183]

Sparta B, Pargett M, Minguet M, Distor K, Bell G, and Albeck JG (2015). Receptor Level Mechanisms Are Required for Epidermal Growth Factor (EGF)-stimulated Extracellular Signal-regulated Kinase (ERK) Activity Pulses. J Biol Chem 290, 24784–24792. [PubMed: 26304118]

Tay S, Hughey JJ, Lee TK, Lipniacki T, Quake SR, and Covert MW (2010). Single-cell NF-kappaB dynamics reveal digital activation and analogue information processing. Nature 466, 267–271. [PubMed: 20581820]

Timmer J, Haussier S, Lauk M, and Lucking CH (2000). Pathological tremors: Deterministic chaos or nonlinear stochastic oscillators? Chaos 10, 278–288. [PubMed: 12779383]

Tran H, Brunet A, Grenier JM, Datta SR, Fornace AJ, Jr., DiStefano PS, Chiang LW, and Greenberg ME (2002). DNA repair pathway stimulated by the forkhead transcription factor FOXO3a through the Gadd45 protein. Science 296, 530–534. [PubMed: 11964479]

Traverse S, Seedorf K, Paterson H, Marshall CJ, Cohen P, and Ullrich A (1994). EGF triggers neuronal differentiation of PC12 cells that overexpress the EGF receptor. Curr Biol 4, 694–701. [PubMed: 7953555]

van der Horst A, and Burgering BM (2007). Stressing the role of FoxO proteins in lifespan and disease. Nature reviews Molecular cell biology 8, 440–450. [PubMed: 17522590]

Yang JY, Zong CS, Xia W, Yamaguchi H, Ding Q, Xie X, Lang JY, Lai CC, Chang CJ, Huang WC, et al. (2008). ERK promotes tumorigenesis by inhibiting FOXO3a via MDM2-mediated degradation. Nature cell biology 10, 138–148. [PubMed: 18204439]

Yu CF, Liu ZX, and Cantley LG (2002). ERK negatively regulates the epidermal growth factor-mediated interaction of Gab1 and the phosphatidylinositol 3-kinase. J Biol Chem 277, 19382–19388. [PubMed: 11896055]

HIGHLIGHTS

- Ligand-stimulated FoxO3 nuclear-cytosolic shuttling is pulsatile not oscillatory
- FoxO3 dynamics can encode growth factor identities and concentrations
- FoxO3 dynamics are under combinatorial control by the ERK and Akt pathways
- Diversity of FoxO3 dynamics is lost in cells with ERK and AKT pathway mutations

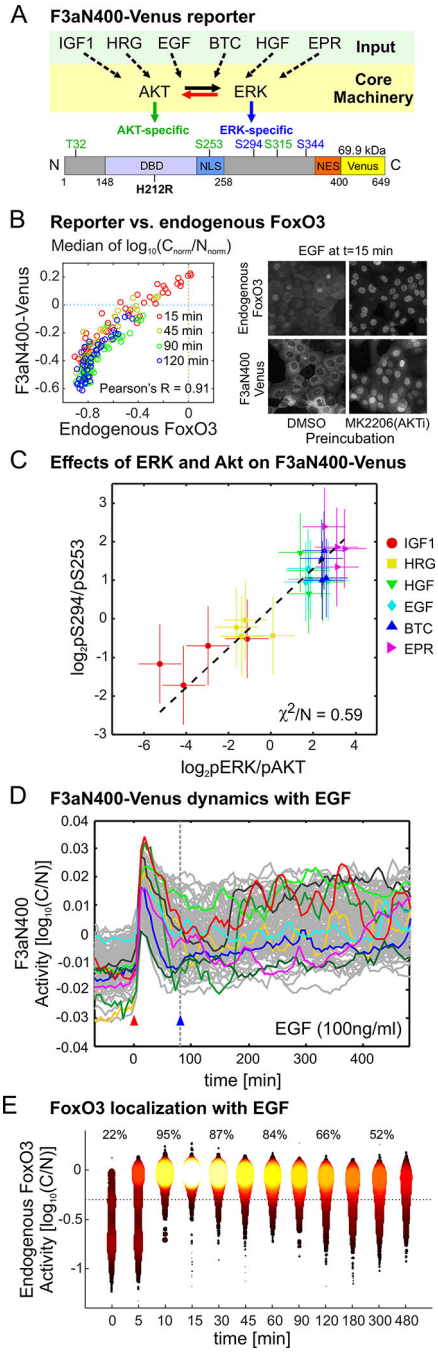

Figure 1. Design and characterization of the F3aN400 reporter with growth-factor stimulation.

(A) Schematic of the F3aN400-Venus reporter and its upstream activators. mVenus Fluorescent Protein was fused to residues 1–400 of native human FoxO3, which contained Akt-dependent T32, S253 and S315 (green) and ERK-dependent S294 and S344 (blue) phosphorylation sites but lacked the transactivation domain. An H212R mutation inactivated DNA binding and prevented dominant negative effects on endogenous FoxO3.

(B) Comparison of endogenous FoxO3 and F3aN400-Venus localization. Parental and reporter-expressing cells 184A1 cells were pre-treated with Akt1/2/3 inhibitor (MK2206; at

8 doses from 0–1μM) for 1 hour prior to EGF stimulation (at 6 doses from 0.4–100 ng/mL). Parental cells were immunostained with anti-FoxO3 antibody and reporter-expressing cells imaged directly. Data were collected at 15 (red datapoints), 45 (yellow), 90 (green), and 120 (blue) minutes. Each datapoint represents the median of translocation, calculated from $\log_{10}$ of the normalized cytoplasmic/nuclear intensity ratio (C_{norm}/N_{norm}). Right panels show example images for both types of cells treated with DMSO or MK2206 (at 1 μM) prior to EGF stimulation (100 ng/mL).

(C) Relationship between the $pERK^{T202/Y204}$-to-$pAkt^{S473}$ phosphorylation ratio, a surrogate for relative ERK and Akt activity and the relative phosphorylation of the reporter (the $pF3aN400^{S294}$-Venus to $pF3aN400^{S253}$-Venus ratio) in cells exposed to 100 ng/mL growth factor at four time points from 15–480 minutes. Error bars represent propagated errors from two biological replicates (See STAR Methods for complete details). Also refer to Figure S1G and Table S1 for complete dataset.

(D) Single-cell trajectories of F3aN400-Venus translocation in 184A1 cells imaged every 5 minutes following exposure to 100 ng/mL EGF. Red arrowhead marks the time of ligand addition (t=0). Ten randomly selected of ~100 total trajectories are highlighted in color. Blue arrowhead at t=80 minutes denotes end of synchronous translocation.

(E) Density plots (>1000 cells per time point) showing the localization of endogenous FoxO3 based on immunostaining at different times after 100 ng/mL EGF addition. Percentages of cells with $\log_{10}$(C/N) above the cutoff (dotted line) are shown above.

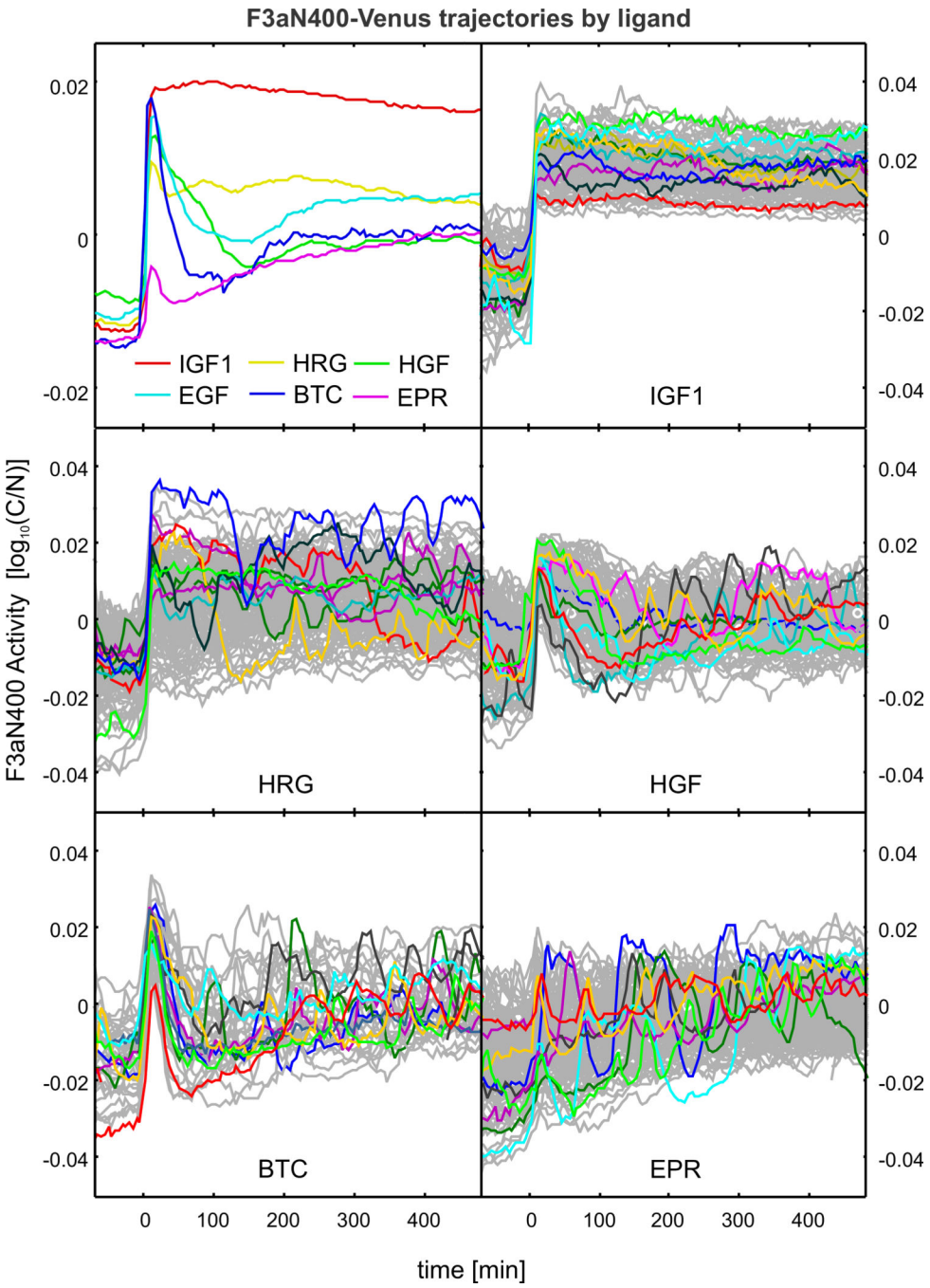

Figure 2. Growth-factor stimulated dynamics of F3aN400-Venus translocation.

F3aN400-Venus translocation dynamics following exposure of 184A1 cells to IGF1, HRG, HGF, BTC and EPR at 100 ng/mL. Top-left panel depicts the average of >100 trajectories per ligand and other panels show single-cell trajectories; 10 randomly selected trajectories are highlighted in color.

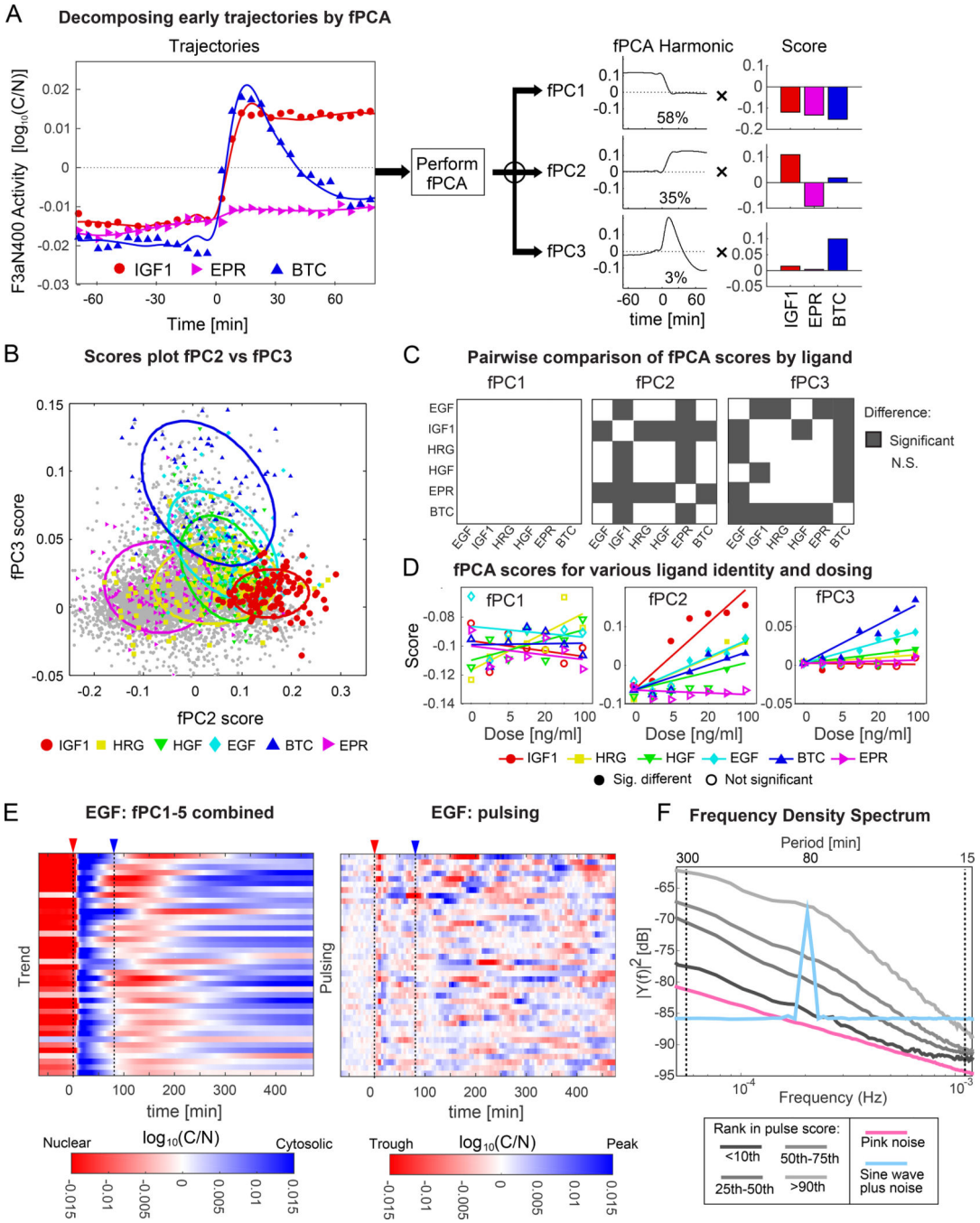

Figure 3. Early synchronous response of F3aN400-Venus translocation varies with growth factor identity.

(A) Schematic of fPCA performed on F3aN400-Venus trajectories between t = −70 to 80 minutes. Three example trajectories are shown on the left, fPC1, fPC2 and fPC3 harmonics in the middle and score plots on the right. fPC1 corresponds to a pre-treatment baseline harmonic, fPC2, a post-treatment sustained harmonic and fPC3, a post-treatment transient harmonic. fPC1–3 explain 58%, 35% and 3% of observed variance across all ligands (respectively).

(B) Plot of fPC2 vs. fPC3 scores for six growth factors at 100 ng/mL. Large oval regions represent 95% confidence intervals for scores computed for all trajectories on a per-growth factor basis.
(C) Pair-wise comparison of fPCA scores by growth factor; significant differences are highlighted in gray (p- value $<10^{-10}$; Wilcoxon rank sum test).
(D) Median values of fPCA scores from different growth factors at various concentrations, fitted with linear models (solid lines). Datapoints with significantly different scores from untreated controls are depicted as solid points while those with p-value$>10^{-10}$ are depicted as unfilled points. See also Figure S2B.
(E) Heat maps of 40 randomly chosen F3aN400 trajectories in 184A1 cells treated with 100ng/mL EGF. Left panel shows 'trend' response generated by combining the first 5 harmonics from fPCA analysis on a per-trajectory basis. Right panel subtracts the computed trend from experimental trajectories revealing pulsing. Red and blue arrowheads denote t=0 and t=80 minutes (see Figure 1D for comparison).
(F) Spectral density analysis of detrended F3aN400 trajectories ranked by pulse score (grey lines; see Figure 4 for method used to calculate pulsing). The spectrum for a simple sinusoid with sampling noise similar to that of experimental data is shown in light blue line and simulated pink noise in pink line are shown for comparison.

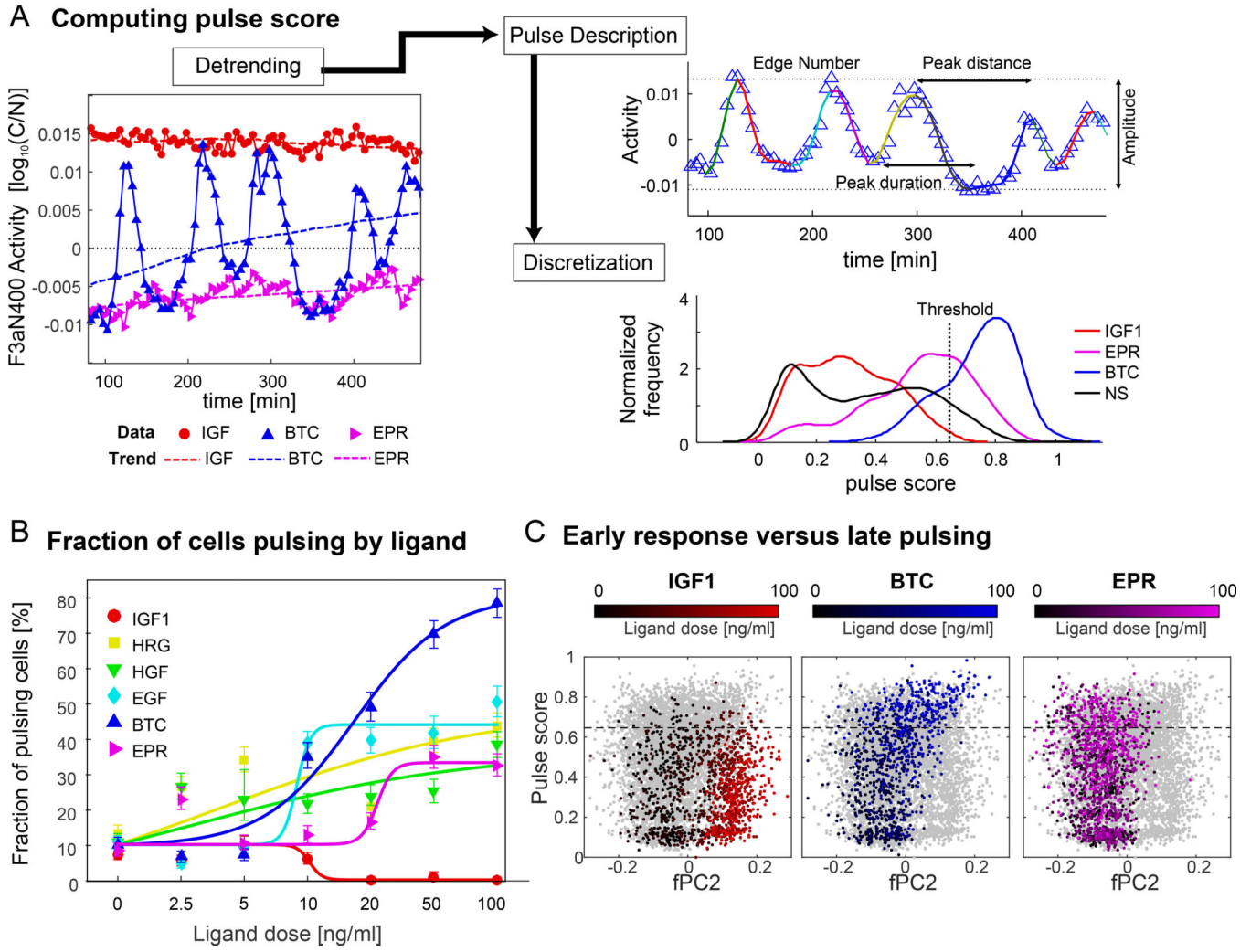

Figure 4. Late pulsing of F3aN400 translocation also exhibits ligand-dependent dynamics.

(A) Schematic of method used to compute pulse scores. Right panel: F3aN400-Venus trajectories for three ligands (each at 100 ng/mL) detrending between t=80 and 1580 min by fPCA on a per-trajectory basis (dotted lines represents the computed trends). Upper left panel: Computing pulse score using a peak detection algorithm and pulse score calculated from a nonlinear combination of the (1) number of edges, (2) amplitude, (3) signal-tonoise ratio (not shown), (4) peak duration and (5) peak distance. See details in STAR Methods. Lower left panel. Discretization of pulse scores; dotted line depicts a threshold at ~0.6.

(B) Fraction of cells with pulsing F3aN400-Venus reporter based on ligand dose and identity, as scored by the algorithm described in panel A. Solid lines show fitted trends based on Hill's equation.

(C) Comparison of fPC2 versus pulse score for trajectories collected from cells exposed to IGF1, BTC and EPR. Shading represents ligand concentration, ranging from lowest (0 ng/mL, black dots) to highest (100 ng/mL, colored dots). Light gray data points represent all other conditions. Dotted lines depict the pulse threshold for discretization.

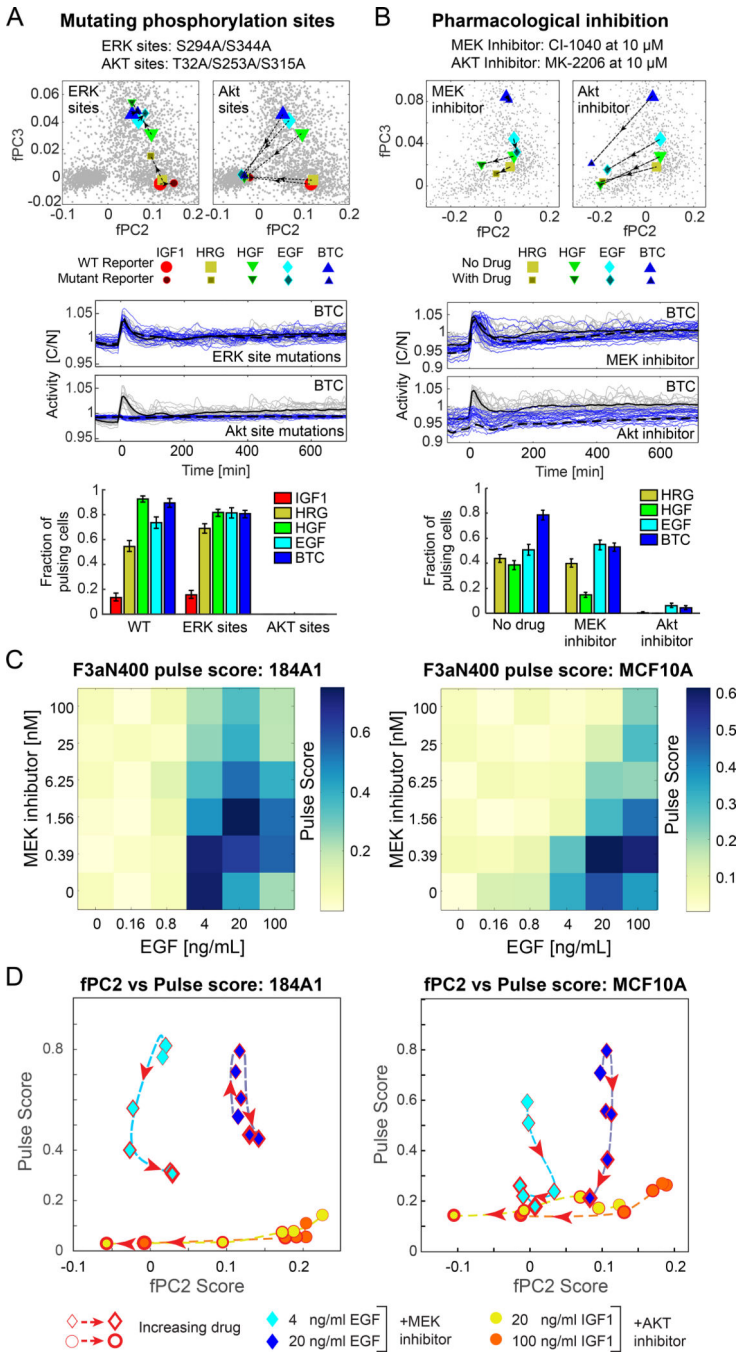

Figure 5. ERK/Akt combinatorial regulation on FoxO3 dynamical encoding.

(A, B) Effects on F3aN400-Venus dynamics in 184A1 cells with (A) mutations in phosphorylation sites or (B) MEK and AKT inhibitors. Top panels: early response in an fPC2-vs-fPC3 landscape for multiple ligands; arrows depict change from wild type to mutant reporter (or with and without drug). Middle panels: trajectories for reporters without (gray) or with (blue) phospho-site mutants or drugs in BTC-treated cells. Lower panels: pulse scores for multiple ligands (error bars represent standard deviations from bootstrapping). See Figure S4B for MCF10A data.

(C) Averaged pulse scores (for >100 trajectories per condition) in F3aN400-Venus expressing 184A1 and MCF10A cell lines pre-treated with the MEK inhibitor PD0325901 at 0–100 nM for 1 hour and subsequently exposed to EGF at 0–100 ng/mL.
(D) Plot of fPC2 vs. pulse score for 184A1 or MCF10a cells pre-treated with the MEK inhibitor PD0325901 at five doses (0.39, 1.56, 6.25, 25, 100 nM) or Akt inhibitor MK-2206 at four doses (6.25, 25, 100, 500 nM) and then with EGF at 4 ng/mL (cyan diamond) or 20 ng/mL (blue diamond) or IGF 1 at 20 ng/mL (yellow circles) or 100 ng/mL (orange circles), respectively. Directional arrows and the thickness of the outlines denote increasing drug concentration.

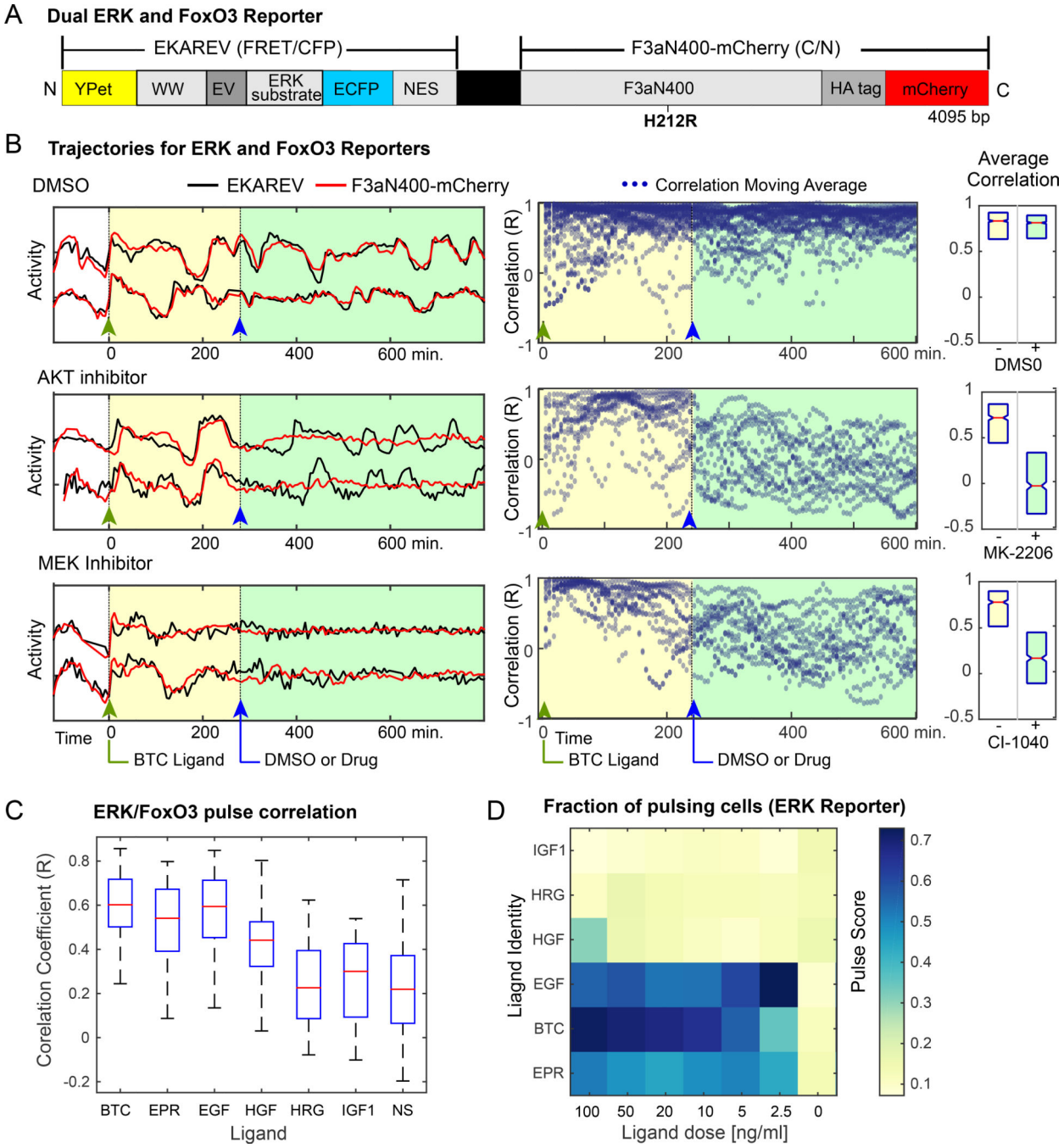

Figure 6. In-phase pulsing of ERK activity and FoxO3 translocation.

(A) Schematic of a dual reporter for ERK (EKAREV) and FoxO3 (F3aN400) linked via a P2A self-cleaving peptide. EKAREV activity was quantified from the FRET/CFP signal ratio and F3aN400-mCherry by C/N ratio.

(B) Detrended trajectories (scaled by max-min range to facilitate comparison) for EKAREV (black) and F3aN400-mCherry (red) in serum-starved MCF10A cells expressing the dual reporter construct. Cells were exposed at t= 0 hr (denoted by green arrowhead) to 100 ng/mL BTC followed at t = 4 hr (blue arrowhead) by DMSO, Akt inhibitor (1 μM MK-2206), or

MEK inhibitor (1 μM CI-1040). Correlation coefficients (middle panels) were calculated using a ~90 min. sliding window and median scores across all trajectories (right panels) were compared prior to (yellow) and after drug exposure (green).

(C) Correlation coefficients for EKAREV activity and F3aN400 translocation pulsing in cells exposed to different growth factors at 100 ng/mL.

(D) Fraction of pulsing cells based on the EKAREV reporter following stimulation with different growth factors and doses.

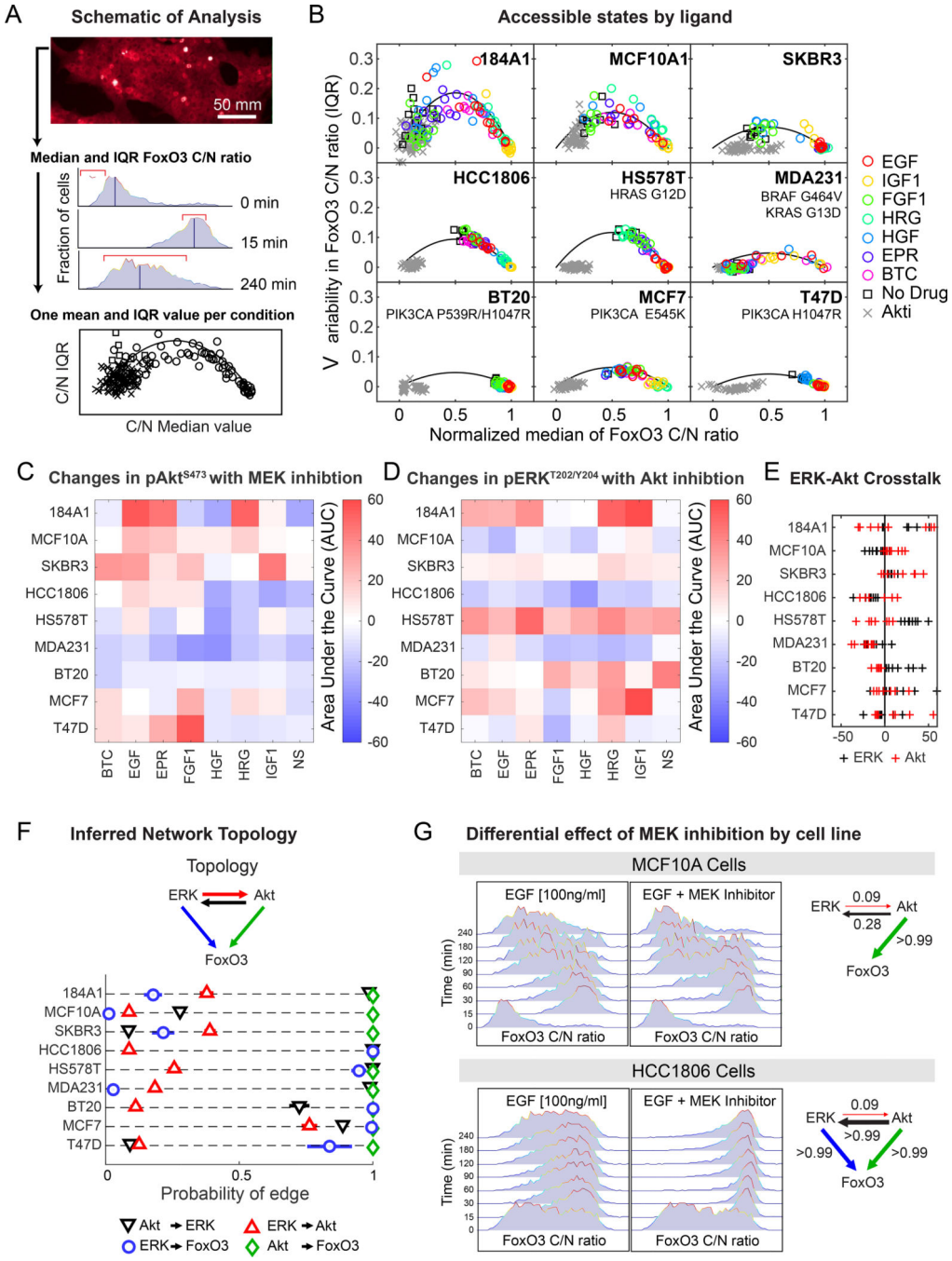

Figure 7. Diversity of interactions among ERK, Akt and FoxO3 in breast cancer cell lines.

(A) Schematic of FoxO3 analysis in cancer cell lines by immunofluorescence imaging. Median C/N ratio captures overall activity and interquartile range (IQR) the extent of cell-to-cell variability, which arises in part from pulsing. Values were obtained from >1000 fixed cells per condition; see STAR Methods for details on normalization methods.

(B) Relationship between median values and IQR of FoxO3 C/N ratios across breast cancer cell lines. Cells were serum-starved and pre-treated with DMSO or 10 μM MK2206 for 1 hour and then exposed to growth factors at 100 ng/mL followed by immunostaining with

anti-pERK$^{T202/Y204}$, anti-pAkt^{S473} or anti-FoxO3 antibodies. Each datapoint corresponds to one post-treatment time point.

(C-D) Heatmap showing effect of MEK inhibition (CI1040, 10 μM) on the area under the curve of pAKT^{S473} levels or of AKT inhibition (MK2206, 10 μM) on the area under the curve of pERK$^{T202/Y204}$ levels 0–240 min for each cell line/ligand combination.

(E) Crosstalk between the ERK and Akt pathways. Changes in pERK$^{T202/Y204}$ levels caused by Akt inhibitor (black data points) or changes in pAKT^{S473} levels caused by MEK inhibitor (red data points) for each ligand and cell line combination.

(F) Dynamic Bayesian network (DBN) modeling of data described in panels B and E to infer the probability of Akt→ FoxO3, ERK → FoxO3 and Akt ↔ ERK edges. The resulted edge probabilities are shown in the bottom panel with error bars indicating the standard deviation of predictions across multiple independent runs with noise added to the data. See also Figure S7 for similar analyses using BGe and BDe scoring methods.

(G) Comparison of FoxO3 translocation dynamics between HCC1806 and MCF10A cells exposed to 100 ng/mL EGF with and without MEK inhibitor. Diagrams on the right show corresponding probabilities from DBN analysis for each edge interaction as calculated in panel F.

KEY RESOURCES TABLE

REAGENT or RESOURCE	SOURCE	IDENT
Antibodies		
Rabbit monoclonal anti-phospho-Akt (Ser473) (D9E)	Cell Signaling (CST)	Cat#43
Rabbit monoclonal anti-phospho-Akt (Ser473) (D9E)	Cell Signaling (CST)	Cat#40
Rabbit polyclonal anti-phospho-FoxO3a (Ser253)	Cell Signaling (CST)	Cat#94
Rabbit polyclonal anti-phospho-FoxO3a (Ser294)	Cell Signaling (CST)	Cat#55
Rabbit monoclonal anti-FoxO3a (75D8)	Cell Signaling (CST)	Cat#24
Mouse monoclonal anti-ß-Actin (Clone AC-74)	Sigma-Aldrich	Cat#A2
Goat polyclonal anti-Rabbit IgG (H+L) conjugated with Alexa Fluor 680	Thermo Fisher	Cat#A3
Goat polyclonal anti-Mouse IgG (H+L) conjugated with Alexa Fluor 800	Thermo Fisher	Cat#A3
Bacterial and Virus Strains		
Biological Samples		
Chemicals, Peptides, and Recombinant Proteins		
Recombinant Human Epidermal growth factor	PeproTech	Cat#AF
Recombinant Human Betacellulin	PeproTech	Cat#10
Recombinant Human Epiregulin	PeproTech	Cat#10
Recombinant Human HGF	PeproTech	Cat#10
Recombinant Human Heregulin	PeproTech	Cat#10
Recombinant Human IGF-1	PeproTech	Cat#AF
MK-2206 AKT 1/2/3 inhibitor	Selleck Chemicals	Cat#S1
Cholera Toxin	Sigma-Aldrich	Cat#C8
Hydrocortisone	Sigma-Aldrich	Cat#H0
Insulin	Sigma-Aldrich	Cat#I9
Bovine Serum Albumin	Sigma-Aldrich	Cat#A7
Heat Inactivated Horse Serum	Life Technologies	Cat#26
Puromycin	Life Technologies	Cat#A1
Fugene HD	Promega	Cat#E2
DMEM/F-12 1:1	Life Technologies	Cat#11
CI-1040 MEK1/2 inhibitor	Selleck Chemicals	Cat#S1
PD0325901 MEK1/2 inhibitor	Selleck Chemicals	Cat#S1
Critical Commercial Assays		
Gibson Assembly	New England BioLabs	E2611
Deposited Data		
Raw images	This paper; OMERO	https://
Raw data for generating all plots in the paper	This paper	doi:65f
Experimental Models: Cell Lines		
184A1	Gift from D. Lauffenburger	
MCF10A	ATCC	ATCC

REAGENT or RESOURCE	SOURCE	IDENT
HCC1806	ATCC	ATCC
BT-20	ATCC	ATCC
MDA-MB-231	ATCC	ATCC
T47D	ATCC	ATCC
Hs578T	ATCC	ATCC
MCF7	ATCC	ATCC
SKBR3	ATCC	ATCC
Experimental Models: Organisms/Strains		
Oligonucleotides		
EKAREV-forward PCR primer :CTGTCTCATCATTTTGGCAAAG	This paper	N/A
EKAREV-reverse PCR primer :CACGTCGCCGGCCTGCTTCAGCAGGCTGAAGTTGGTGGCGCCGCTGCCATCCAGAGTCAGGCGTTCC	This paper	N/A
mCherry-forward PCR primer:CCCATACGATGTTCCAGATTACGCTGGAGGATCCGGGGGTTCTATGGTGAGCAAGGGCGAGG	This paper	N/A
mCherry-reverse PCR primer:CTGACACACATTCCACAGGGTCGACTTACTTGTACAGCTCGTCCATG	This paper	N/A
F3aN400-forward PCR primer:TTCAGCCTGCTGAAGCAGGCCGGCGACGTGGAGGAGAACCCCGGCCCCATGGCCGAAGCCCCC	This paper	N/A
F3aN400-reverse PCR primer: CTCCAGCGTAATCTGGAACATC	This paper	N/A
Recombinant DNA		
Plasmid: pPB-CAG-EKAREV	(Albeck et al., 2013; Komatsu et al., 2011)	
Plasmid: pMSCV-puro-F3aN400-Venus	This paper	Pendin
Plasmid: pPB-CAG-F3aN400-HA-Venus-P2A-NLS-Myc- mCherry	This paper	Pendin
Plasmid: pPB-CAG-EKAREV-P2A-F3aN400-HA- mCherry	This paper	Pendin
Plasmid: ERK-silent F3aN400-HA-Venus (with S294A/S344A)	This paper	Pendin
Plasmid: an AKT-silent F3aN400-HA-Venus (with T32A/S253A/S315A)	This paper	Pendin
Plasmid: pPB-CAG.EBNXN	A. Bradley, Sanger Institute	
Plasmid: pCMV-hyPBase transposase vector	A. Bradley, Sanger Institute	
Plasmid: pcDNA3-H2B-mCherry	(Nam and Benezra, 2009)	Addge
Software and Algorithms		
Scripts for all quantitative analysis in this paper	This paper	https://
Functional data analysis MATLAB package	J. Ramsay	http://w
MATLAB	Mathworks	
CellProfiler	(Kamentsky et al., 2011)	http://c
Other		
Resource website for data public sharing of LINCS compatible dataset	This paper	http://li